



Cite this: DOI: 10.1039/d0ta03749d

From isolated Ti-oxo clusters to infinite Ti-oxo chains and sheets: recent advances in photoactive Ti-based MOFs

Yu Yan,^{†a} Changqing Li,^{†a} Yuhang Wu,^a Junkuo Gao^{ID}*^a and Qichun Zhang^{ID}*^{bc}

Metal–organic frameworks (MOFs) have emerged as a significant class of porous crystalline materials constructed from metal nodes and multidentate linkers. Many research studies have shown the promising applications of MOFs in gas adsorption and separation, electrocatalysis, photocatalysis, biomedicine etc., mainly due to the advantages of high porosity, large surface areas and easily tunable optical and electronic structures. Particularly, light-sensitive Ti-oxo clusters in Ti-based MOFs result in promising photocatalytic activity. Recently, a few Ti–carboxylate MOFs based on infinite Ti-oxo chains and sheets were reported, which open a new horizon for the photocatalytic activity of Ti-MOF chemistry. This review highlights some typical Ti-MOFs based on discrete Ti-oxo clusters and recent progress in the fabrication of Ti-MOFs based on infinite Ti-oxo chains and sheets. Moreover, facile modification methods for improving the photocatalytic activity under visible light irradiation are exemplified in detail. We hope that the photocatalytic applications of Ti-MOFs in photocatalytic H₂ generation, photocatalytic reduction of CO₂, dye photodegradation, photocatalytic alcohol oxidation and photocatalytic polymerization will benefit researchers who are interested in this field.

Received 5th April 2020

Accepted 26th May 2020

DOI: 10.1039/d0ta03749d

rsc.li/materials-a

1. Introduction

Environmental pollution and global warming have threatened human life all over the world. One of the most promising solutions to address these issues is to utilize artificial photosynthetic systems based on cost-efficient particulate photocatalysts.^{1–7} In order to mimic natural photosynthesis systems

by performing photocatalytic organic transformation, photocatalytic water splitting and photocatalytic reduction of CO₂, it is highly desirable to develop a single material serving as an ideal platform with the combination of photosensitizers and catalytic centres in one crystalline lattice.^{8–14} Upon sunlight irradiation, photosensitizers of this semiconductor harvest light and electrons are transferred from the valence band (VB) to

^aLab of Functional Porous Materials, School of Materials Science and Engineering, Zhejiang Sci-Tech University, Hangzhou 310018, China. E-mail: jkgao@zstu.edu.cn

^bSchool of Materials Science and Engineering, Nanyang Technological University, Singapore 639798, Singapore. E-mail: qc Zhang@ntu.edu.sg

^cDepartment of Materials Science and Engineering, City University of Hong Kong, Kowloon, Hong Kong SAR, China. E-mail: qic Zhang@cityu.edu.hk

† These authors contributed equally to this paper.



Yu Yan was born in Sichuan, China. He received his BS (2016) degree from the Southwest University of Science and Technology in China. Currently, he is a graduate student at Zhejiang Sci-Tech University under the guidance of Prof. Gao, working on metal–organic frameworks for solar energy utilization.



Changqing Li was born in Shanxi, China. He received his BS (2016) degree and MS (2019) degree from Zhejiang Sci-Tech University in China under the supervision of Prof. Junkuo Gao. His current research is mainly focused on the synthesis of MOFs and their photo/electrochemical applications.

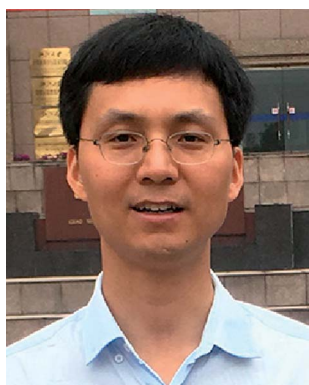
the conduction band (CB), reaching a state of charge separation. The reduction and oxidation of half reactions occur at the excited catalytic centers, to which the charge carriers migrate from the initial site. Pioneering studies of photocatalytic H₂ generation and reduction of CO₂ manifest that TiO₂,^{15,16} as a promising candidate for photocatalysis, can uncover a new avenue for developing a heterogeneous photocatalytic system mainly due to its low cost, high photoactivity, good stability and easy fabrication. Recently, TiO₂ has become the hot spot for solar energy conversion.^{17–22} However, the unsatisfactory large band gap of TiO₂ (3.2 eV) limits its utilization of solar energy only in the UV region, which only accounts for 4% of solar energy. The development of photocatalysts that can be photoactive in the visible light region is quite essential to efficiently utilize solar energy.

Inspired by the general catalytic strategy in zeolites that heterogeneous catalyst possessing a high porosity can achieve efficient mass transfer from the exterior of pore structure to its interior and serve as size- and shape-selective heterogeneous catalyst, metal–organic frameworks (MOFs) have attracted tremendous attention in the past few decades due to the advantages of high porosity, large surface areas and easily

tunable optical and electronic structures.^{23–29} MOFs consist of multipodal organic ligands and metal nodes, achieving a synergistic combination of merits inherent to each constituent, which have spurred applications in the field of gas storage and separation,^{30–36} catalysis,^{37–46} sensing,^{47–53} energy storage,^{54–62} and biomedicine.^{63–66} The characteristics of tunable open metal centers, functional organic ligands and encapsulation of guests in MOF pores provide multiple active sites for the synergistic catalysis. Compared with other inorganic semiconductors (metal oxides and metal chalcogenides),^{67–72} MOFs possess high accessible surface areas.^{73,74} Furthermore, the pore size and environment of MOFs can be modulated. Upon light irradiation, organic linkers which act as antenna chromophores, characterized by delocalized orbitals *via* conjugated π -bonds, can transfer charge to metal-oxo clusters at the beginning of the photoredox activity. Varying metal oxide nodes like Fe-oxo clusters or organic linkers like $-\text{NH}_2$ substituted aromatic compounds can shift the response of MOFs towards the visible light region.^{75–78} With metal nanoparticles (MNPs) encapsulated in the pores acting as electron traps and active reaction sites, the lifetime of the charge-separated state is conveniently prolonged, and the charge separation, which is hazardous to photocatalytic activities, can be efficiently controlled.^{79–82} Taking these merits into account, MOFs can become ideal platforms for efficient photocatalysis.^{83–97} The high photoactive properties of the Ti component from Ti⁴⁺ to reduced Ti³⁺ under light irradiation makes Ti-based MOFs promising candidates for photocatalysts, mainly due to their high photoactivity. Moreover, the affinities and compatibility of coordination between Ti cations and oxygenated ligands allow a diversity of Ti-oxo clusters to be used as excellent precursors for elaborating sophisticated extended topological networks. However, the discovery of Ti-MOFs is confined to the spontaneous and uncontrolled hydrolysis of Ti precursors, and thus, only a limited number (about 30 new structures) of Ti-MOFs were reported among more than 70 000 reported MOF structures.⁹⁸ Besides, Ti-



Yuhang Wu was born 1993 in Zhejiang, China. He is now a PhD candidate working with Prof. Junkuo Gao at Zhejiang Sci-Tech University. His current research interest focuses on metal–organic framework derivatives for energy conversion applications.



Junkuo Gao is now a Qianjiang Scholar Distinguished Professor at Zhejiang Sci-Tech University, China. He received his BS (2005) degree and PhD (2010) from Zhejiang University in China under the supervision of Prof. Guodong Qian. He worked with Prof. Hans Agren at the Royal Institute of Technology (KTH), Sweden and Prof. Qichun Zhang at Nanyang Technological University, Singapore as a post-

doctoral fellow during 2010–2013. His research interest is related to functional porous materials including metal–organic frameworks (MOFs) and hydrogen-bonded organic frameworks (HOFs) for photo/electrocatalysis and gas separation. Till now, he has published more than 110 papers (H-index: 37).



Qichun Zhang is an Associate Professor at the School of Materials Science and Engineering and at Nanyang Technological University, Singapore. His research focuses on conjugated rich carbon materials and their applications. Currently, he is an associate editor for J. Solid State Chemistry, Advisory board member of Materials Chemistry Frontiers, Chemistry-an Asian Journal, Journal of Materials

Chemistry C, and Inorganic Chemistry Frontiers. He also is a fellow of the Royal Society of Chemistry. In 2018 and 2019, he was recognized as one of the highly cited researchers (top 1%) in the cross-field category of Clarivate Analytics. Till now, he has published more than 348 papers (H-index: 71) and 4 patents.

oxo clusters, isolated by organic ligands, can't provide an adequate orbital overlap to support the migration of charge carriers. Scientists recently have developed a variety of Ti-MOFs based on infinite Ti-oxo chains and sheets and confirmed that increasing the dimensionality of secondary building units (SBUs) can efficiently enhance the charge mobility and thus the photocatalytic activity, which sheds some light on the development of highly efficient photocatalysts for different applications.^{99,100}

In this review, we will mainly focus on the recent progress in the preparation and applications of typical Ti-MOFs with single Ti centers, discrete Ti-oxo clusters, infinite Ti-oxo chains, and Ti-oxo sheets as building blocks. Especially, novel topological structures and the highly visible-light-responsive photocatalytic activities of Ti-MOFs based on consecutive Ti-oxo chains and sheets will be discussed in more detail, because we believe that these parts might foreshadow these scientists who are willing to devote their contribution to the discoveries of new Ti-MOF materials. Meanwhile, several strategies for improving solar conversion are also concluded. Hopefully, this review will be of interest to scientists who want to catch a glimpse of this field for future work.

2. The development of Ti-MOFs based on isolated Ti-oxo clusters

From the 1990s to the present, many methodologies such as hydro/solvothermal,^{101–104} electrochemical,^{105–109} microwave,^{110–113}

mechanosynthesis,^{114–116} and surfactant-thermal^{117–123} methods have been developed to prepare MOFs. However, the progress in the synthesis of porous crystalline titanium-based frameworks is considerably slow. Though the first microporous Ti-based MOF, named MIL-91(Ti), has been discussed due to its unique topology, which even illuminates the synthesis of the single crystal of its aluminum analogues,¹²⁴ the major attention was only focused on the elaboration of Ti-oxo clusters as a precursor to realize hybrid assemblies, where the intrinsic properties of Ti-oxo clusters and organic constituents are retained. Later, the limited study of Ti-oxo cluster derivatives, which is devoted to the synergetic combination with polymer matrices as nano-objects, is comparable to the poor advances on Ti-based MOFs. With the deep investigation of the rich versatility of Ti-oxo clusters,^{125–135} more and more researchers try to explore whether the polyhedron of Ti-oxo clusters, as the superlattice of TiO₂, can be spatially aligned with multi-topic organic ligands (especially polycarboxylic ligands), as antenna chromophores, to construct a well-defined porous coordination network. However, the research on Ti-based MOFs is quite slow due to two main problems during the synthesis of Ti-based MOFs: (1) titanium sources such as TiCl₄ and Ti(i-OPr)₄ are highly reactive and can be easily hydrolyzed into TiO₂ in solvents, which makes the reactions difficult to control; and (2) Ti-carboxylate bonds are difficult to form making the rearrangement of Ti-oxo clusters arduous, leading to the poor

Table 1 Summary of reported Ti-MOFs

Name	Ti source	Ligands	Ti-O connection	Band gap (eV)	Porosity (m ² g ⁻¹)	Ref.
NTU-9	Ti(i-OPr) ₄	H ₄ DOBDC	TiO ₆	1.72	642	144
MIL-167	Ti(i-OPr) ₄	H ₄ DOBDC	TiO ₆	—	No	145
MIL-168	Ti(i-OPr) ₄	H ₄ DOBDC	TiO ₆	—	No	145
MIL-169	Ti ₄ O ₄ (ox) ₇ (pipH ₂) ₃	H ₄ DOBDC	TiO ₆	—	No	145
Ti-CAT-5	Ti(i-OPr) ₄	H ₆ THO	TiO ₆	—	450	146
MUV-11	Ti(i-OPr) ₄	H ₄ bdha	TiO ₆	2.00	756	147
MOF-217	Ti(i-OPr) ₄	TDHT	TiO ₆	—	—	148
1-Ti	TiCl ₄	EA	Ti ₃ O ₂ (PO ₂) ₂ (COO) ₆	2.70	160	149
MIL-101-Ti	TiCl ₃	H ₂ BDC	Ti ₃ O(COO) ₆	—	2970	150
Ti ₃ -BPDC	Ti ₆ O ₆ (AB) ₆ (i-OPr) ₆	BPDC	Ti ₃ (COO) ₆ (OH) ₂	—	636	151
COK-69	Cp ₂ Ti _{IV} Cl ₂	H ₂ CDC	Ti ₃ O(O) ₂ (COO) ₆	3.77	29	152
MOF-901	Ti ₆ O ₆ (AB) ₆ (i-OPr) ₆	BDA	Ti ₆ O ₆ (COO) ₆	2.65	550	153
MOF-902	Ti ₆ O ₆ (AB) ₆ (i-OPr) ₆	BPDA	Ti ₆ O ₆ (COO) ₆	2.50	400	154
PCN-22	Ti ₆ O ₆ (AB) ₆ (i-OPr) ₆	TCPP	Ti ₇ O ₆ (COO) ₁₂	1.93	1284	143
MIL-125	Ti(i-OPr) ₄	H ₂ BDC	Ti ₈ O ₈ (OH) ₄ (COO) ₁₆	3.60	1550	155
NH ₂ -MIL-125	Ti(i-OPr) ₄	H ₂ ATA	Ti ₈ O ₈ (OH) ₄ (COO) ₁₆	2.60	1130	156
MIP-207	Ti(i-OPr) ₄	H ₃ BTC	Ti ₈ O ₈ (OH) ₄ (COO) ₁₆	—	570	157
MIL-177-LT	Ti(i-OPr) ₄	H ₄ mdip	Ti ₁₂ O ₁₅ (COO) ₁₅	—	730	99
MIL-91	TiO ₂ ·H ₂ O	N,N'-Piperazinebismethylene-phosphonic acid	(TiO ₆) _n	—	500	124
MIL-177-HT	Ti(i-OPr) ₄	H ₄ mdip	(Ti ₆ O ₆) _n	3.50	690	99
DGIST-1	Ti ₆ O ₆ (AB) ₆ (i-OPr) ₆	TCPP	(Ti-O) _n	1.85	1957	142
ZSTU-1	Ti(i-OPr) ₄	H ₃ TCA	(Ti ₆ O ₁₂) _n	2.30	536	100
ZSTU-2	Ti(i-OPr) ₄	H ₃ BTB	(Ti ₆ O ₁₂) _n	3.10	628	100
ZSTU-3	Ti(i-OPr) ₄	H ₃ BTCA	(Ti ₆ O ₁₂) _n	2.20	861	100
Ti-TBP	TiCl ₄ ·2THF	TCPP	(Ti ₅ O ₁₂) _n	—	528	158
ACM-1	Ti(i-OPr) ₄	H ₄ TBAPy	(Ti-O ₂) _n	2.30	1212	159
COK-47	Cp ₂ Ti _{IV} Cl ₂	BPDC	(Ti ₂ O ₃) _n sheet	—	573/60	160
PCN-415	Ti(i-OPr) ₄ /ZrCl ₄	BDC	Ti ₈ Zr ₂ O ₁₂ (COO) ₁₆	3.30	1050	161
MUV-10	Ti(i-OPr) ₄ /CaCl ₂	H ₃ BTC	Ti ₂ Ca ₂ (O) ₂ (H ₂ O) ₄ (COO) ₈	3.10	1041	162

NTU-9 by heating the reaction mixtures in sealed glass tubes containing a mixed solvent of 2-propanol and acetonitrile (1 : 1) at 100–120 °C for 24 h.¹⁶³ As shown in Fig. 2, the morphology of NTU-9 is a hexagonal prism and every Ti^{4+} ion is linked to three organic ligands (three hydroxyl groups and three carboxyl groups from three different DOBDC) to generate a TiO_6 cluster. The structure of NTU-9 is a 2D layer with a hcb network, where six Ti–O clusters form hexagonal layers firstly, which further stack together to form a pseudo-3D structure through hydrogen bonding interactions. The layer spacing between the neighboring layers is probably 6 Å, and the size of the 1D channel is about 11 Å. The absorption spectrum of NTU-9 extends from 400 nm to 750 nm with an absorption peak centered at around 520 nm, in agreement with its low band gap (1.74 eV). This bathochromic absorption can be attributed to the higher photonic efficiency of NTU-9, compared with the indirect band gap semiconductor such as TiO_2 . The Brunauer–Emmett–Teller (BET) surface area of NTU-9 is $642 \text{ m}^2 \text{ g}^{-1}$ reported by Chun and co-workers,¹⁶³ after 2-propanol molecules occupying the empty spaces of the channels were completely removed. The polar oxo moieties of the DOBDC linkers can be beneficial to the sorption of H_2 or CO_2 .

Though several members (MIL-167, MIL-168, and MIL-169) with considerable optical features have been added into the NTU-9-like family later, the porosity precluded the improvement of their photocatalytic performance under visible light.¹⁴⁵ Very recently, Padial *et al.* were enlightened by the replacement of carboxylates with phenolate groups which favor the bridge of mononuclear Ti nodes with octahedral coordination.¹⁴⁷ By incorporation with a siderophore-type linker (CONHOH–, a hydroxamic unit), MUV-11 (an analogue of NTU-9 MOF) was prepared by *de novo* synthesis with a surface area close to $760 \text{ m}^2 \text{ g}^{-1}$. The replacement of carboxylic units with nitrogenated hydroxamate linkers not only elongates the pore windows, but also favors the interaction of CO_2 molecules with the surface of the pores resulting in a considerably high absorption of CO_2 . Notably, the employed activation protocol can lead to partial collapse of the 3D structure of MUV-11 by a confused reorganization of the interlayer interaction. Also, anionic hydroxamates can form hard oxo donors to bond to Lewis acids, which endows MUV-11 with remarkably high stability in acid media. The Mott–Schottky plot confirms the p-type conductivity of MUV-11.

The coordination between metal ions and catechol ligands can have a synergistic effect on electrochemical and catalytic properties. Enlightened by this, the first catecholate-based 3D Ti-MOF was reported by Nguyen *et al.* in 2015, named Ti-CAT-5 (CAT represents catecholate).¹⁴⁶ For the synthesis of Ti-CAT-5, H_6THO and NBu_4Br were dissolved in DMF, followed by the addition of $\text{Ti}(\text{i-OPr})_4$. In order to facilitate the deprotonation of H_6THO , amylamine was added. The reaction was conducted in Teflon-lined autoclaves at 180 °C for 40 h. Since the as-obtained single crystal is not good enough for single-crystal X-ray diffraction analysis, its structure was solved through PXRD analysis by comparing with Fe-CAT-5. The as-solved structure indicates that Ti-CAT-5 has a single Ti atom cluster, where a Ti^{4+} cation coordinated with three organic ligands to form a TiO_6 octahedral cluster as the SBU. Further studies revealed a doubly

interpenetrated srs topology of CAT-5. The BET surface area of CAT-5 is about $450 \text{ m}^2 \text{ g}^{-1}$, in which large apertures are occupied by identical interpenetrated networks and organic guests. No significant O–H stretching vibration peaks were observed in the spectrum of Fourier-transform infrared spectroscopy (FTIR), indicating that the H_6THO linkers were fully deprotonated. It is noteworthy that the remarkable proton conductivity of Ti-CAT-5 and its analogue was attributed to the amount and diversity of pore contents (sulfate and DMA). With the increase of relative humidity (RH) and temperature, the proton conductivity of Ti-CAT-5 increased.

2.2 Ti_3 -oxo clusters

To utilize the strong binding ability of phosphonates with metal clusters, Zhu *et al.* prepared a titanium-phosphonate MOF based on Ti_3 -oxo clusters (named TiPNW, also 1-Ti).¹⁴⁹ This 1D titanium-phosphonate-based MOF was prepared *via* facile sol-gel chemistry by using etidronic acid (EA) as the ligand, which features easy post-modifications. Instead of the formation of titanium-phosphonate MOF nanoparticles (TiPNP) through a classical hydrothermal method under static conditions, the self-assembly of titanium phosphonate oligomers along the axial direction leads to an extended 1D nanostructure *via* the shear stress induced by mechanical stirring, which efficiently improves the mass transfer and provides uniform reaction conditions. Although, TiPNW and TiPNP possess identical framework compositions, the surface area of TiPNP ($334 \text{ m}^2 \text{ g}^{-1}$) surpasses that of TiPNW ($160 \text{ m}^2 \text{ g}^{-1}$). The electrochemical impedance spectroscopy (EIS) measurement and the surface photovoltage spectroscopy (SPS) response manifested that the 1D structure consisting of organophosphonic units and Ti-oxo clusters offers a sequential pathway for photonic migration, resulting in efficient electron–hole separation. TiPNW shows a red-shift absorption to cover the visible spectrum compared to pristine TiO_2 . These results further confirm the positive role of organophosphonic groups in adjusting the band gap and harvesting light.

Titanium ions are not always preferred to coordinate in the tetravalent state. Mason *et al.* reported the first Ti^{3+} MOF (named MIL-101-Ti),¹⁵⁰ which is an isorecticular analogue of the famous Fe-MIL-101. Unlike other Ti-MOFs, MIL-101-Ti was synthesized in a glove box by reacting TiCl_3 with 1,4-benzenedicarboxylic acid (BDC) in a mixed solvent of anhydrous DMF and anhydrous methanol at 120 °C for 18 hours. MIL-101-Ti is composed of triangular $\text{Ti}^{\text{III}}_3\text{O}(\text{COO})_6$ clusters and is the first Ti-MOF based on Ti^{3+} -oxo clusters. As to the SBU of MIL-101-Ti, three Ti^{3+} ions coordinate with three BDC ligands to generate a hexagonal window with a bridging oxygen in the middle of the window to connect three titanium ions. The BET surface area of MIL-101-Ti is nearly $2970 \text{ m}^2 \text{ g}^{-1}$. Notwithstanding, the initial absorption suggested that MIL-101-Ti exhibited a weak absorption of H_2 , due to the charge-transfer reactions between O_2 and titanium(III) complexes generating titanium(IV) superoxo and peroxy species. Other measurements further confirmed that the strong magnetic coupling of MIL-101-Ti resulted from the distorted trigonal-bipyramidal geometry of the five-

coordinate Ti^{3+} sites that can efficiently shield nuclear charge and preclude MIL-101-Ti interacting with and polarizing absorbing gas molecules.

Recently, a high-throughput synthetic methodology is used to synthesize a MIL-100 topology based on Ti_3 -oxo clusters,¹⁶⁴ and the BET of this material was found to be $1321 \text{ m}^2 \text{ g}^{-1}$ with a total pore volume of $0.66 \text{ cm}^3 \text{ g}^{-1}$. The surface area lies below that of the reported analogue MIL-100 which was attributed to the formation of an amorphous fraction phase or partial blocking of the pores by molecular precursors. Concerning the different degradation rates of MIL-100-Ti and the Fe analogue under acid conditions, the author predicted that the biomedical applications of the Ti and Fe phases would give different drug delivery kinetics under simulated biological conditions.

By adopting a novel strategy, the identical structures of Ti^{3+} -MIL-100 and Ti^{3+} -MIL-101 were electrosynthesized from the facile Ti^{4+} precursor TiCl_4 instead of the expensive and air-sensitive precursor TiCl_3 .¹⁶⁵ Given the superior quality of those materials compared to the analogue prepared by traditional solvothermal methods, this electrochemically mediated synthesis will open up avenues for the design of novel MOFs containing redox-active metal cations or necessitating preparation under rigorously air-free reaction conditions. The BET surface areas of Ti^{3+} -MIL-100 and Ti^{3+} -MIL-101 were found to be 1304 and $1736 \text{ m}^2 \text{ g}^{-1}$, respectively. Moreover, by utilizing the straightforward electrosynthesis methodology, larger and more well-defined crystalline MIL-100-tatb and MIL-100-BPDC dwarf analogous samples were also prepared. This electrochemical method indeed provides an intriguing strategy for the synthesis of reduced MOFs especially Ti-MOFs with increased crystallinities.

The hydrolysis of titanium salts is a limiting factor in the synthesis of Ti-MOFs. In order to overcome this problem, in 2015, Bueken *et al.* synthesized a new Ti_3 -oxo-based MOF (COK-69, where COK stands for Centrum voor Oppervlaktechemie en Katalyse) by using dicyclopentadienyl titanium(IV) dichloride ($[\text{Cp}_2\text{Ti}_\text{IV}\text{Cl}_2]$) as the Ti precursor to react with *trans*-1,4-cyclohexanedicarboxylate linkers (H_2CDC) in DMF and in the presence of acetic acid as a modulator at $110 \text{ }^\circ\text{C}$ for 48 h under an inert atmosphere.¹⁵² The reduced form of COK-69 (Ti^{III}) was obtained under these synthetic conditions, which can be oxidized to form COK-69 (Ti^{IV}) under the exposure of air. COK-69 employed a triangular Ti_3O cluster as the SBU (Fig. 3). COK-69 has trigonal-bipyramidal cages and 1-D hexagonal channels of about 4.9 \AA (Fig. 3), which belongs to the **asc** topology. Yet, the BET surface area of COK-69 is only $29 \text{ m}^2 \text{ g}^{-1}$. Thermal stability analysis indicates that COK-69 is stable below $240 \text{ }^\circ\text{C}$. By using microwave irradiation, the throughput of COK-69 can be scaled up at the expense of crystalline quality. Interestingly, COK-69 demonstrated a rare breathing behavior, which opens a new horizon for more diverse topologies of Ti-MOFs.

Lin and co-workers reported a colorless rhombic Ti_3 -BPDC (BPDC = biphenyl-4,4'-dicarboxylate) crystal constructed from BPDC ligands and $\text{Ti}_3(\text{OH})_2$ SBUs in 31% yield *via* a solvothermal reaction.¹⁵¹ In $\text{Ti}_3(\text{OH})_2$ SBUs, the central Ti atom coordinates with six carboxylate groups, and each of the two terminal Ti connects with three carboxylate groups and one

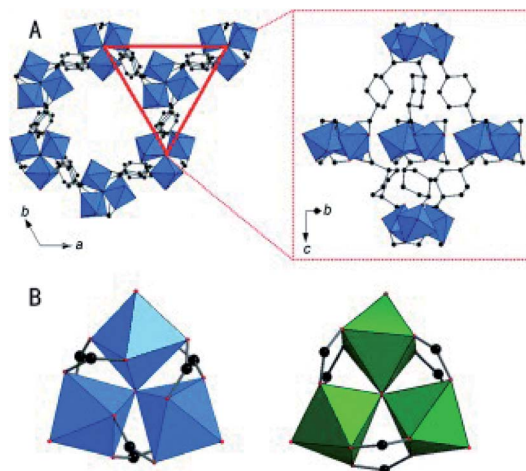


Fig. 3 Structure of as-synthesized COK-69. (A) 1D hexagonal channels are constructed by the stacking of trigonal-bipyramidal cages. (B) The $[\text{Ti}^{\text{IV}}_3\text{O}(\text{O})_2(\text{H}_2\text{O})(\text{COO})_6]$ cluster with tilted TiO_6 (blue) is shown on the left along with the $[\text{Cr}^{\text{III}}_3\text{O}(\text{CU/F})(\text{H}_2\text{O})_2(\text{COO})_6]$ cluster from MIL-88 for comparison (O: red, C: black, and Cr: green). Reprinted with permission from ref. 152. Copyright 2015, WILEY-VCH Verlag GmbH.

–OH group to afford a **dia** topology (Fig. 4). This material exhibits a permanent porosity with a BET surface area of $636 \text{ m}^2 \text{ g}^{-1}$. Lin and co-workers later deprotonated closely spaced Ti–OH groups and chelated with Co^{II} ions, which provides more electron-rich active metal sites and a spatially open coordination environment around metal centers.⁹³ The high catalytically selective activities in the cascade reduction of N-heterocyclic rings of pyridines and quinolines confirmed that the substrate binding is blocked by the channel due to the unfavorable steric repulsion in the reduction of pyridines and the shape-selective heterogeneous catalytic system inhibits substrate coordination to the Co centers in the reduction of quinolines.¹⁶⁶ This work has expanded the application of MOFs in developing single-site solid catalysts by connecting neighboring SBUs to undergo catalysis with chemoselectivity.

2.3 Ti_6 -oxo clusters

The symmetric and compact structure of $\text{Ti}_6\text{O}_6(\text{COO})_6$ clusters is made up of an assembly of two staggered triangular units

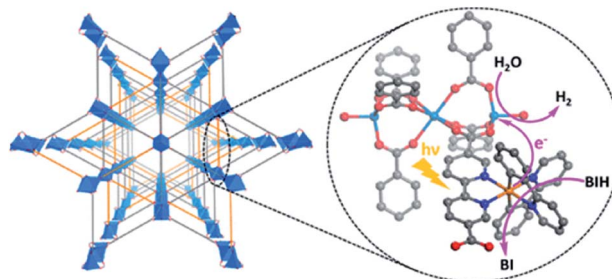


Fig. 4 Schematic showing a photocatalytic HER with Ti_3 -BPDC-Ir *via* electron injection from photoreduced $[\text{Ir}^{\text{III}}(\text{pppy})_2(\text{dcbpy}^{\bullet-\bullet})]^0$ ligands into $\text{Ti}_3(\text{OH})_2$ SBUs. Ti, Ir, O, and N atoms are shown in blue, gold, red, and mazarine, respectively. Adapted with permission from ref. 151. Copyright 2019, American Chemical Society.

built by sharing vertices of the octahedra, where each titanium center is surrounded by three $\mu_3\text{-O}$, two $-\text{OOCR}$ and one $-\text{OCH}_3$ group. To substitute $-\text{OOCR}$ with other $-\text{OOCR}'$ groups, the $\text{Ti}_6\text{O}_6(\text{COO})_6$ cluster has been widely used in inorganic reactions.^{126,167,168} To take advantage of the symmetry of the $\text{Ti}_6\text{O}_6(-\text{COO})_6$ cluster, the hexameric Ti-oxo cluster $\text{Ti}_6\text{O}_6(\text{AB})_6(\text{i-OPr})_6$ was used to elaborate MOF-901 (ref. 153) and MOF-902 (ref. 154) (Fig. 5) by using a strategy that combines the chemistry of MOFs and covalent organic frameworks (COFs) according to Nguyen's report. $\text{Ti}_6\text{O}_6(\text{AB})_6(\text{i-OPr})_6$ was formed *in situ* in methanol and then benzene-1,4-dialdehyde (BDA) or 4,4'-biphenyldicarboxaldehyde (BPDA) was linked to the $\text{Ti}_6\text{O}_6(\text{AB})_6(\text{i-OPr})_6$ clusters using imine condensation reactions to generate MOF-901 and MOF-902, respectively. The BET surface areas of MOF-901 and MOF-902 are $550 \text{ m}^2 \text{ g}^{-1}$ and $400 \text{ m}^2 \text{ g}^{-1}$, respectively, indicating that MOF-902 has a smaller BET surface area than MOF-901, although MOF-902 showed larger porous windows, which might be filled by some organic ligands. Structural analysis of the powder of MIL-901 revealed that it can be described as perforated 2D layers with triangular apertures, leading to a hxl topology. In comparison with the absorption spectrum of MOF-901 ranging from 340 to 550 nm with a maximum located at 360 nm, MOF-902 exhibits a bathochromic optical absorption band, ranging from 340 to 640 nm with a maximum at 390 nm, which is in agreement with the higher conjugated longer organic ligand BPDC.

2.4 Ti-oxo clusters with larger size

Given that porphyrin and metalloporphyrin with ubiquitous biological functions can serve as ligands, porphyrin-based MOFs have drawn much attention.^{169–175} Taking advantage of the high photoactivity of the porphyrin antenna, Yuan *et al.* employed a hexameric titanium-oxo cluster ($\text{Ti}_6\text{O}_6(\text{AB})_6(\text{i-OPr})_6$ (AB = 4-aminobenzoate)) as a Ti precursor to react with TCPP in DEF at 150°C for 48 h to generate a new Ti-MOF PCN-22 (ref.

143) (PCN stands for Porous Coordination Network) (Fig. 6). The usage of the $\text{Ti}_6\text{O}_6(\text{AB})_6(\text{i-OPr})_6$ cluster can efficiently diminish the hydrolysis of Ti ions and slow down the crystallization process. Also, the addition of excess benzoic acid as the modulator is important to obtain high quality crystals, because the excess benzoic acid could further decrease the growth speed of MOFs. Note that no crystalline products were obtained under identical conditions if $\text{Ti}(\text{i-OPr})_4$ or TiCl_4 was used as the precursor. Interestingly, during the crystal growth, the rearrangement of a pair of Ti_3O_3 clusters could form a new Ti_7O_6 cluster in the framework of PCN-22. Each Ti_3O_3 cluster connects six TCPP to form 2D layers, which can be further linked together by Ti^{4+} cations to form a porous 3D structure. The as-formed structure has a quadrangle with a window size of about 1.5 nm and the BET surface area is $1284 \text{ m}^2 \text{ g}^{-1}$. The calculated band gap of PCN-22 is 1.93 eV, indicating that PCN-22 can harvest visible light to induce photocatalysis.

The building unit of the $\text{Ti}_8\text{O}_8(\text{COO})_{16}$ cluster consists of eight octahedral metal atoms and sixteen carboxylates, where two carboxylates connect two different Ti octahedrons with two neighboring clusters to form a ring of octahedral metal atoms, which is one member of first-row transition metal complexes with a ring shape.^{176,177} The first Ti-carboxylate MOF ($\text{Ti}_8\text{O}_8(\text{OH})_4-(\text{O}_2\text{C}-\text{C}_6\text{H}_4-\text{CO}_2)_6$), named MIL-125, was reported by Férey and co-workers.¹⁵⁵ MIL-125 was solvothermally synthesized through terephthalic acid (BDC) and $\text{Ti}(\text{i-OPr})_4$ at 150°C for 15 hours. The inventor creatively used a mixed solvent containing methanol and DMF. Note that the addition of methanol can suppress the hydrolysis of titanium salts and increase the possibility of the crystallization of MIL-125.

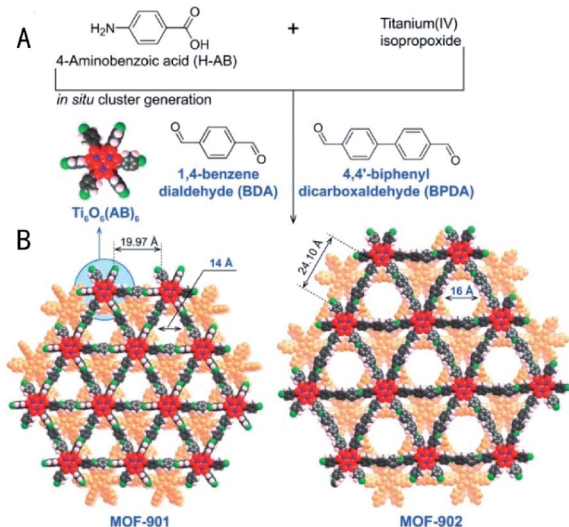


Fig. 5 Synthesis of MOF-901 and MOF-902. Adapted with permission from ref. 154. Copyright 2017, American Chemical Society.

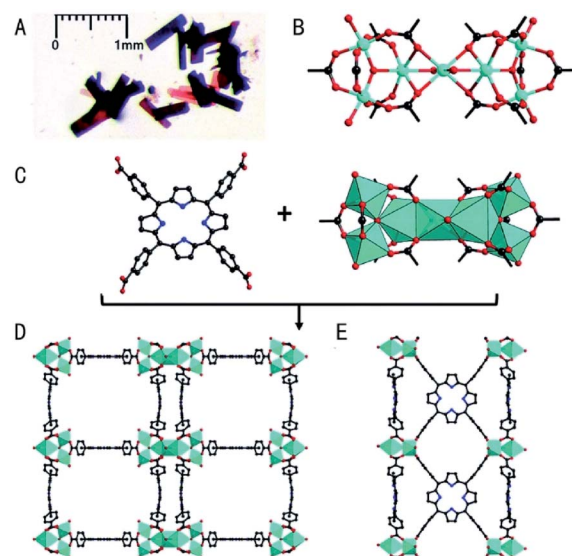


Fig. 6 (A) Microscope image of PCN-22 crystals. (B) Structure of the Ti_7O_6 cluster (only O atoms of DEF molecules are shown for clarity). (C) Representation of the tetratopic TCPP linker (left) and 12-connected Ti_7O_6 cluster (right). Views of the structure of PCN-22 along the (D) *a*-axis and (E) *b*-axis. Color scheme: red O; black C; blue N; and cyan Ti. H atoms are omitted for clarity. Reprinted with permission from ref. 143. Copyright 2015, The Royal Society of Chemistry.

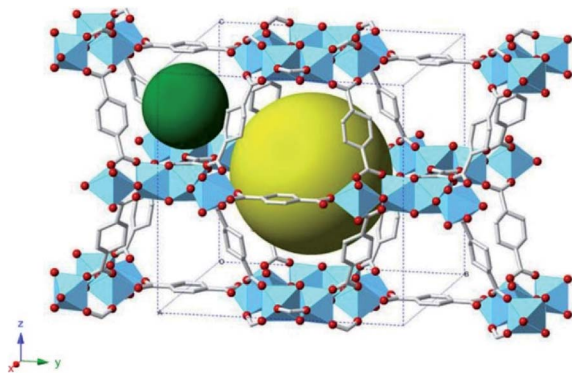


Fig. 7 Crystalline structure of MIL-125 with two different cages. Reprinted with permission from ref. 178. Copyright 2013, Elsevier B.V.

Unfortunately, the as-obtained MIL-125 (Fig. 7) was still in the microcrystalline state, from which the structure can be obtained through the simulation of its powder X-ray diffraction (PXRD) data.¹⁷⁸ As the earliest and most typical Ti-based MOF, MIL-125 possesses eight corner or edge-sharing Ti–O octahedra to form $\text{Ti}_8\text{O}_8(\text{OOCR})_{12}$ clusters through eight bridging oxygens. Its 3D framework consists of eight triangles forming an octahedron, which belongs to the **fcu** topology. This porous 3D quasicubic tetragonal structure has two types of cages, an octahedral (12.55 Å) and a tetrahedral (6.13 Å) cage, accessible through narrow triangular windows of *ca.* 6 Å. The lattice parameters were convergent with $a = b = 18.6453$ Å and $c = 18.1444$ Å. MIL-125 has a good thermal stability below 300 °C, and the BET surface area could up to 1500 $\text{m}^2 \text{g}^{-1}$. Later on, an amine-functionalized Ti-MOF, named NH_2 -MIL-125,¹⁵⁶ was synthesized with H_2ATA as a linker. The analogous MIL-125 structure was confirmed by the XRD patterns, and the incorporation of the $-\text{NH}_2$ group shows an extra absorption band in the visible light region with the absorption edge extending to 550 nm compared to the narrow optical absorption of MIL-125 with absorption near UV. The architectural stability and permanent porosity of NH_2 -MIL-125 were confirmed by the N_2 absorption/desorption isotherms with the BET and Langmuir surface areas of 1302 and 1719 $\text{m}^2 \text{g}^{-1}$, respectively.

Through linker exchange with a Ti_8O_8 cluster precursor while preserving the connection and configuration of the Ti_8O_8 core, a new microporous Ti-based MOF (MIP-207) was reported by Wang *et al.* *via* using BTC as an organic ligand.¹⁵⁷ MIP-207 was synthesized *via* direct ligand exchange between the BTC ligand and the terminal monocarboxylate species of a Ti_8O_8 cluster precursor (Ti_8 -acetate-formate) under solvothermal conditions. Note that MIP-207 can also be synthesized by the assembly of the *in situ* generated Ti_8O_8 cluster and BTC in a reflux reaction, providing a concise and facile synthetic method for scale-up production. Nitrogen sorption isotherms confirmed the BET surface area and pore volume of this material to be 570 $\text{m}^2 \text{g}^{-1}$ and 0.34 $\text{cm}^3 \text{g}^{-1}$, respectively. The meta-connection mode of BTC in MIP-207, which leaves one free carboxylic group pointing toward the pore, allows the partial substitution of the BTC linker by different isophthalic acids.

The linker substitution in MIP-207 not only changes the chemical environment in the cavity, but also produces a pronounced adjustment of the pore volume and the surface area, which further modulates the separation performance of N_2/CO_2 . The utilization of formic acid and acetic acid in the preparation of this material also demonstrates that both acids can be modulators in the preparation of Ti-MOFs.

To obtain a high ratio of oxo-groups to Ti^{4+} ions in the inorganic building blocks for Ti-MOFs, Wang *et al.* presented a robust 3D mdip-based Ti-MOF, named MIL-177-LT, which was prepared *via* an easily scalable synthesis through refluxing a mixture of $\text{Ti}(\text{i-OPr})_4$ and H_4mdip in formic acid under ambient pressure.⁹⁹ MIL-177-LT consisted of a $\text{Ti}_{12}\text{O}_{15}$ cluster SBU with a considerable high O/Ti condensation degree of 1.25 which is a critical parameter for the evaluation of properties in contrast to TiO_2 , surpassing that of all aforementioned Ti-MOFs. XRD and density functional theory (DFT) revealed that each multidentate acid bridges four Ti-oxo clusters, where formate not only connects pairs of adjacent Ti ions in the cyclic hexamer, but also affords the combination of SBUs along the *c* axis and the characteristics of a bnn topology. Permanent N_2 porosity confirms a BET area of 730 $\text{m}^2 \text{g}^{-1}$. Nevertheless, MIL-177-LT features an excellent chemical stability under extremely acidic conditions compared to previous reported Ti-MOFs based on isolated Ti-oxo clusters, including aqua regia and concentrated H_3PO_4 .

2.5 Heterometallic Ti/M-oxo clusters

Considering the spontaneous hydrolysis of Ti clusters and that heterometallic clusters combining two or more metals can outperform monometallic counterparts in many applications, Yuan *et al.* discovered a new type of specific Ti/Zr mixed metal oxide node to synthesize a family of isoreticular photoactive MOFs, connected by BDC and 2,6-naphthalenedicarboxylate (NDC), termed PCN-415 and PCN-416.¹⁶¹ The structure of the $\text{Ti}_8\text{Zr}_2\text{O}_{12}(\text{COO})_{16}$ cluster is similar to that of the $\text{Zr}_6\text{O}_4(\text{OH})_4(\text{COO})_{12}$ cluster by substituting four equatorial Zr^{4+} with a Ti_8 -cube, which can be used as a nearly ideal templating scaffold for the construction of different MOFs regardless of the variation of synthetic conditions. N_2 sorption measurements revealed that PCN-415 and PCN-416 are highly porous with BET surface areas of 1050 and 1337 $\text{m}^2 \text{g}^{-1}$. Later, by introducing amino groups onto the BDC linker, PCN-415- NH_2 showed an obvious red-shift of absorption peaks and a narrower band gap in contrast to PCN-415. By comparison with UiO-66, the enhanced photocatalytic performance is attributed to the formation of Ti^{3+} , which allows long-lived charge separation.

After these research studies, a new chemically robust single-crystalline photoactive Ti-based MOF (named MUV-10) based on heterometallic SBUs was synthesized through a reaction between titanium isopropoxide, calcium chloride and BTC in DMF with acetic acid as a modulator.¹⁶² The BET surface area of MUV-10 was found to be 1041 $\text{m}^2 \text{g}^{-1}$. The $\text{Ti}_2\text{-Ca}_2(\text{O})_2(\text{H}_2\text{O})_4(\text{COO})_8$ SBU consists of six-coordinated octahedral Ti^{4+} and Ca^{2+} centres with a trigonal prismatic geometry, which is bridged with eight neighbouring SBUs by eight BTC

linkers, to give a characteristic of a **the** network. MUV-10 exhibits remarkable stability that allows it to be used in drastic conditions during catalytic tests. In contrast to metal doping in post-synthetic metal exchange, this work makes the anchoring of dopants at the atomic level possible, providing a new approach to improve the photocatalytic performance.

3. The development of Ti-MOFs based on infinite Ti-oxo chains and sheets

The poor charge mobility of MOFs results from the discrete metal-oxo clusters which could not provide an adequate orbital overlap for the migration of charge carriers, limiting the improvement of their photocatalytic activities.¹⁷⁹ Charge carriers can preferentially migrate through an adequate orbital overlap produced by a CB within a continuous cluster chain. Also, early studies showed that the efficiency of charge separation of the long axis in TiO₂ nanorods or nanotubes is much higher compared to that of the nanoparticles.¹⁸⁰ Recent research indicated that extending the dimensionality of Ti-oxo chemistry from isolated Ti-oxo clusters to infinite chains and sheets can efficiently enhance the charge mobility and thus the photocatalytic activity.^{99,100} However, such examples are rare. Thus, designing and exploring new types of highly photoactive Ti-MOFs consisting of infinite chains and sheets are very important and highly desirable.

As the first porous MOF based on titanium diphosphate, MIL-91 was synthesized by using *N,N*-piperazinebismethylenephosphonate as the ligand in aqueous solution.¹²⁴ In its simulated structure, Ti is octahedrally coordinated with six O atoms to form TiO₆, which is further connected together to form Ti-O chains along the *b*-axis through sharing the corners. MIL-91 has well-defined 1D porous channels with a diameter of about 4 Å and a BET surface area of 430 m² g⁻¹. The reminiscent tancoite architecture has been demonstrated to show an excellent capability of carbon dioxide capture.

Though titanium phosphonate is firstly constituted by infinite Ti-oxo chains, the main attention was focused on the high nuclearity and coordination number of Ti-oxo carboxylate clusters as well as the preparation of the diverse structures of Ti-MOFs. Recently, Wang *et al.* reported a new Ti-MOF based on infinite Ti-oxo chains, where MIL-177-LT with Ti₁₂-oxo clusters can be transformed into an unusual irreversible phase MIL-177-HT with an ultrathin 1D infinite Ti-oxo nanowire.⁹⁹ MIL-177-HT consists of edge-sharing trigonal pyramidal Ti₆O₉ clusters with an O/Ti condensation of 1.5 after thermal disposal, where the terminal and bridging formates in the original structure of MIL-177-LT were removed. The H₄mdip linkers equally bridge the neighboring ultrathin Ti-oxo nanowires to form a 3D framework (Fig. 8). With a slight decrease of BET in contrast to original MIL-177-LT, MIL-177-HT retained the large hexagonal channels with a BET area of 690 m² g⁻¹. The band gap is calculated to be 3.5 eV for MIL-177-HT. MIL-177-HT is the first photoconductive MOF, which is even comparable to that of well-known nano-sized TiO₂ due to the infinite Ti-oxo chain rather than photoactive organic linkers. When doping with different metals and retaining the Ti-oxo nanowire array in their structure, MIL-177-HT composites with iron doping can achieve a nearly four orders of magnitude improvement of electrically conductive performance. MIL-177-HT also features notable photoconductivity with a polymer composite (polythiophene) in contrast to other reported Ti-MOFs based on discrete Ti-oxo clusters and even original MIL-177-LT. This remarkable difference can be attributed to the increased charge separation and excellent long-distance charge delocalization of the MIL-177-HT composite, where accommodated polymer chains and Ti-oxo chains could provide an aligned ambipolar conduction pathway for charge migration. Indeed, this ground-breaking work promoted the study of photoactive Ti-MOFs based on infinite Ti-oxo chains.

Keum *et al.* prepared a dark red-brown microcrystal as DGIST-1 *via* optimizing the synthetic conditions of PCN-22.¹⁴² Single-crystal XRD analysis revealed that each Ti^{IV} atom was octahedrally coordinated with four O atoms originating from four TCPP linkers and two μ₂-O atoms, forming an infinite Ti-

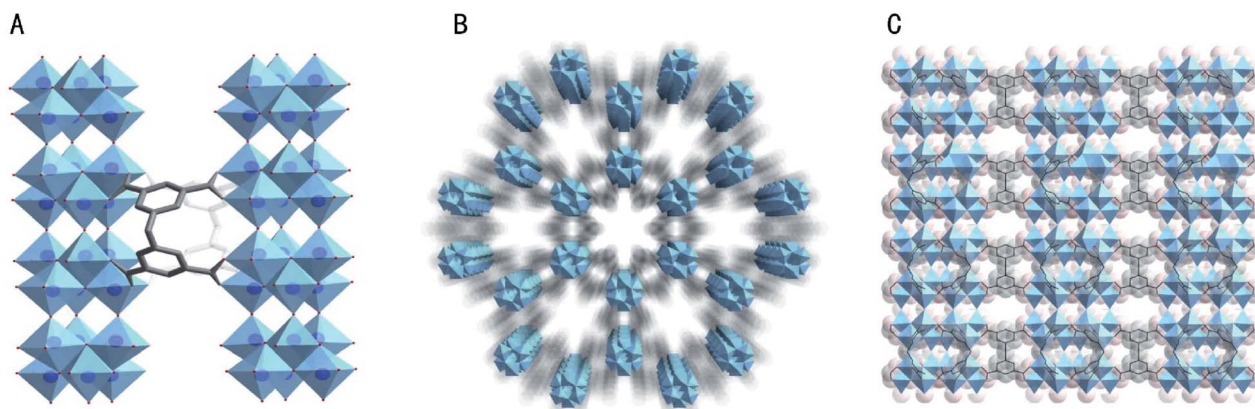


Fig. 8 (A) Adjacent infinite ultrathin (Ti₆O₉)_n nanowires with a thickness of ca. 1 nm connected by mdip linkers (in gray). (B) Channels in the (Ti₆O₉)_n nanowire array running along the *c*-axis with a diameter of ca. 0.9 nm. (C) Small channels of 0.3 nm windows retained when viewed along the *b*-axis of the MIL-177-HT crystal structure. Reprinted with permission from ref. 99. Copyright 2019, Springer Nature.

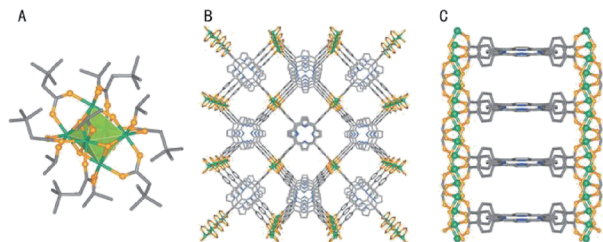


Fig. 9 Crystal structures of the $\text{Ti}_6\text{O}_6(\text{i-OPr})_6(\text{t-BA})_6$ cluster and (B) DGIST-1 along (A) the b -axis and (C) the c -axis. Green, Ti; yellow, O; blue, N; gray, C. H atoms are omitted for clarity. Reprinted with permission from ref. 142. Copyright 2019, WILEY-VCH Verlag GmbH.

oxo chain, which is assembled with TCPP into a 3D framework. It should also be noted that the distance between two TCPP linkers which is linearly aligned is equal to the distance of two neighboring Ti^{IV} centers along the Ti-oxo chain (Fig. 9). After the removal of guest solvents, the porous structure of DGIST-1 was confirmed by nitrogen sorption isotherms with a BET surface area of $1957.3 \text{ m}^2 \text{ g}^{-1}$, which surpasses that of the isostructural Al-PMOF ($1400 \text{ m}^2 \text{ g}^{-1}$). The band gap of DGIST-1 was calculated to be 1.85 eV, slightly lower than that of PCN-22 (1.93 eV). 1,3-Diphenylisobenzofuran (DPBF) as a singlet oxygen ($^1\text{O}_2$) scavenger was used to examine the generation of $^1\text{O}_2$ under visible light irradiation. The results proved that in the presence of DGIST-1, the superoxide (O_2^-) can be traced accounting for the bathochromic shift of the spectra upon the decomposition of DPBF. $^1\text{O}_2$ and O_2^- can be simultaneously generated by the synergistic effect of the Ti-oxo chain and the TCPP linker as efficient reactive oxygen species for photocatalytic reactions upon visible light irradiation. The high surface area and extraordinary photoredox properties may enable the utilization of DGIST-1 in various photocatalytic applications.

To elongate the life time of excited states and enhance the photocatalytic properties, Gao and co-workers designed a series of Ti-MOFs (named ZSTU-1 to 3) based on infinite Ti-oxo rods with tunable porosities and optoelectronic properties.¹⁰⁰ ZSTUs (Fig. 10) were prepared from tritopic carboxylate ligands with strong electron-donating behavior and $\text{Ti}(\text{i-OPr})_4$ in DMF at relatively high temperature (180°C). It is noteworthy that their porosities systematically increase with longer and larger tri-carboxylic linkers as light harvesters. As empirically expected, ZSTU-1 and ZSTU-3 constructed from triphenylamino-based ligands can extend broader light absorption and exhibit better photocatalytic performance than ZSTU-2. Quite similar to the aforementioned infinite $(\text{Ti}_6\text{O}_9)_n$ nanowire of MIL-177-HT, the hexagonal shaped $\text{Ti}_6(\mu_3\text{-O})_6$ subunits are connected by the triangular linkers to form a 2D larger structure along the c axis, where these $\text{Ti}_6(\mu_3\text{-O})_6$ clusters are further bridged by six $\mu_2\text{-OH}$ groups to generate infinite 1D nanorods with the characteristic of a kagome topological network. The BET surface areas of ZSTU-1, ZSTU-2 and ZSTU-3 are about $536 \text{ m}^2 \text{ g}^{-1}$, $628 \text{ m}^2 \text{ g}^{-1}$ and $861 \text{ m}^2 \text{ g}^{-1}$, respectively. The band gaps of ZSTU-1, ZSTU-2 and ZSTU-3 are calculated to be 2.3 eV, 3.1 eV and 2.2 eV, respectively, where the lower band gap of ZSTU-3 compared to ZSTU-1 accounts for the stronger conjugated

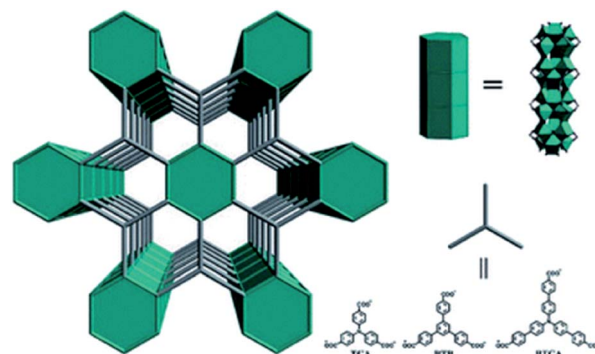


Fig. 10 Schematic illustration of three isorecticular Ti-MOFs with 1D rods of variable pore size from three different tritopic carboxylate ligands. Adapted with permission from ref. 100. Copyright 2019, American Chemical Society.

effect of the organic ligand in ZSTU-3. The investigation of the excited state dynamics also revealed that the elongated extension of ligands can increase their optical absorption. This methodology can be further extended to the large range of aromatic linkers used in the synthesis of MOFs, which should enable accurate and predictable control over the band gap of tailored frameworks.

To generate more reactive oxygen species for biological utilization in Ti-MOFs, Lin and co-workers synthesized a new porphyrin-based Ti-MOF (Ti-TBP) based on an infinite Ti-oxo chain.¹⁵⁸ Ti-TBP was synthesized *via* a solvothermal reaction between $\text{TiCl}_4 \cdot 2\text{THF}$ and 5,10,15,20-tetra(*p*-benzoato)porphyrin

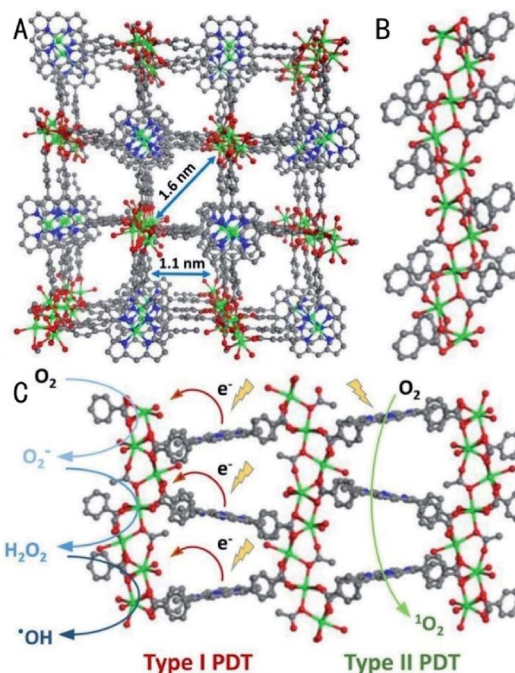


Fig. 11 (A) Perspective view of the Ti-(Ti-TBP) structure along the (010) direction. (B) Coordination environments of Ti-oxo chain SBUs. (C) Schematic showing both type I and type II PDT enabled by Ti-TBP. Adapted with permission from ref. 158. Copyright 2019, American Chemical Society.

(H₄TBP) in DMF with acetic acid as the modulator. Single crystal X-ray diffraction studies revealed that the *in situ* formed Ti-coordinated TBP ligands (Ti·TBP) were connected by infinite (Ti₅O₁₂)_n chains to form a 3D framework with a BET surface area of 527.7 m² g⁻¹ (Fig. 11). TEM and atomic force microscopy (AFM) images confirmed that Ti-TBP consists of square nanoplates with a diameter of 150 nm and thickness of 20 nm. The distance between two neighboring lattice points in high resolution TEM (HRTEM) agrees well with the distance between the centers of two neighboring Ti-oxo chains. Upon light irradiation, Ti⁴⁺ centers of Ti-TBP not only can be reduced to Ti³⁺, but also further reduce O₂ to facilitate the generation of superoxide. The proximity of Ti-oxo chains to porphyrin-based ligands may provide a notable strategy to the implement of Ti-MOF in biological chemistry.

Given the synergy between H₄TBAPy (H₄TBAPy stands for 4,4',4'',4'''-pyrene-1,3,6,8-tetrayl-tetrabenzoic acid) featuring a wide visible absorption region and Ti ions may give rise to a MOF with considerably high photocatalytic activity, Gascon and coworkers synthesized a new MOF (named ACM-1) with infinite Ti-oxo chains by a one-step reaction in a solvent mixture of dry DEF and chlorobenzene, by using propionic acid as the modulator.¹⁵⁹ The cell parameters of ACM-1 are identical to those of a previously reported In³⁺ based MOF, ROD-7, only with the difference that μ₂-OH groups in ROD-7 are replaced by shared μ₂-O in ACM-1, which is characteristic of a sea topology. The nitrogen isotherm confirms the microporosity of ACM-1 with a BET surface area of 1212 m² g⁻¹ and a pore volume of 0.55 m³ g⁻¹. Femtosecond transient absorption (fs-TA) spectroscopy studies of ACM-1 and ligand H₄TBAPy further elucidated the longer charge separation lifetime of ACM-1 with a low optical band gap of 2.30 eV, which is a prerequisite element for enhancing photocatalytic performance. The strong PL quenching of ACM-1 compared to ROD-7 revealed the efficient charge transfer from the ligand to the Ti-oxo infinite chain.

A novel Ti-MOF (named COK-47) based on Ti-oxo sheets was reported by Smolders *et al.* to extend the dimensionality of Ti-oxo connections to 2D.¹⁶⁰ The Ti-oxo sheet contains double chains of edge-sharing TiO₆ octahedra that are bridged by μ₂-O atoms. The Ti-oxo sheets are connected by biphenyldicarboxylate (BPDC) ligands to form a 3D porous structure (Fig. 12). The reaction at a lower concentration and lower temperature yields larger crystals (named COK-47_L), which is more convenient for structural analysis. The measured BET surface area of COK-47_L and COK-47_S is 60 m² g⁻¹ and 573 m² g⁻¹, respectively. The discrepancy of their porosity is attributed to the deliberately induced missing linker defects under the drastic synthesis conditions of COK-47_S. COK-47_S, featuring defect-rich Ti-oxo sheets, exhibited excellent catalytic activity in contrast to COK-47_L (41.1 × 10⁻³ min⁻¹ vs. 3.6 × 10⁻³ min⁻¹) for the oxidation of dibenzothiphene (DBT).

4. Photocatalytic applications of Ti-MOFs

4.1 Band gap engineering

In the case of the existence of Ti³⁺-Ti⁴⁺ intervalence charge transfer in the Ti-oxo cluster or Ti-oxo chain and sheet, Ti-MOFs

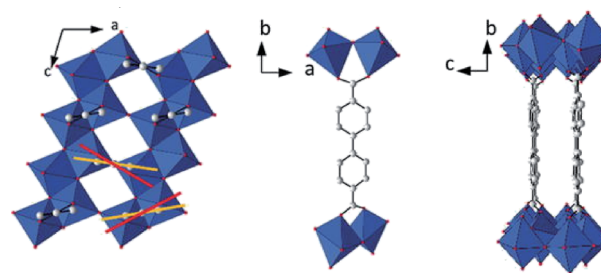


Fig. 12 Representation of the COK-47 structure along the *a* (right) and *b* (left) directions. Red lines indicate the orientation of the carboxylates and orange lines show the phenyl ring alignment. The linker connects corner- and edge-sharing octahedron pairs from neighbouring layers (middle). Reprinted with permission from ref. 160. Copyright 2019, WILEY-VCH Verlag GmbH.

have spurred tremendous applications in the fields of heterogeneous photocatalytic systems. Considering that Ti-MOFs contain Ti-oxo SBUs, discrete organic linkers, coordinatively unsaturated metal centres, functional ligands and even guest species such as MNPs can be active sites in synergistic catalysis and tandem reactions.⁴¹ It is of importance to figure out the general structural requirements for Ti-MOFs suitable for heterogeneous photocatalysis. Although, transition metals in a nanometric particle can confine the excitation when the particle size is commensurate with the mobility of charge carriers, the isolated Ti-oxo cluster is too far away to fulfil the Mott transition conditions.^{77,181} Also, the distance between the neighbouring organic linkers is too large to allow efficient π-π stacking and provide sufficient orbital overlapping, resulting in electrons preferentially in a localized state (Frenkel).¹⁸² Organic linkers serve as sets of individual discrete light absorption antennas, and once light is excited, the electron of organic linkers will migrate to the CB and a hole will be left in the VB of the origin sites. The band gap is the crucial factor determining the efficiency of this ligand-to-metal cluster charge transfer (LMCT) mechanism. It is clear that narrowing the band gap can decrease the thermodynamic cost for shifting light absorption to the visible light spectrum.¹⁸³ Poor charge mobility detrimental to the photoresponsive ability may lead to fast charge recombination. Rationalizing the choice of appropriate Ti precursors and organic ligands is vital to develop an efficient heterogeneous photocatalytic system. Discovering new Ti-MOFs is not the only way to elevate the performance of photocatalysts. By substitution of the amino group, the absorption edge of NH₂-MIL-125 was found at 2.6 eV against 3.6 eV of MIL-125. Photoluminescence (PL) studies and UV/vis spectra confirmed that the amino groups protruded into the micropore can extend the light absorption, which can be a proof that -NH₂ substituted linkers as building units can remarkably improve the photocatalytic activity.

To further elucidate the specific role of the diaminated linker BDC-(NH₂)₂ and other functional groups (-OH, -Cl, and -CH₃) in the optical response, Hendon *et al.* successfully achieved tailored MIL-125 towards absorption in the visible range *via* grafting a suitable substituted group on phenyl rings.¹⁸⁴ When

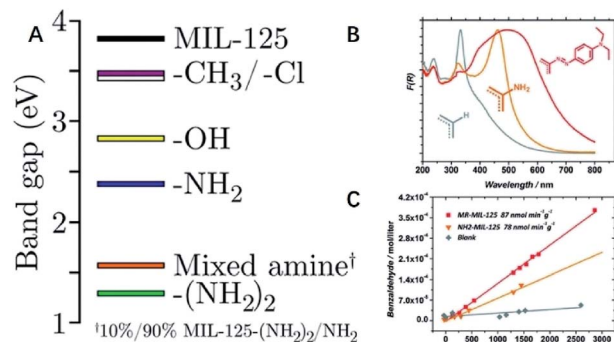


Fig. 13 (A) HSE06-predicted band gaps of MIL-125 (black) and its analogues containing functionalized BDC linkers. Substitution of ca. 10% (*i.e.*, one functionalized linker per unit cell) was made, unless otherwise stated. Control of the band gap was achieved by varying the substituent. Reprinted with permission from ref. 184. Copyright 2013, The Royal Society of Chemistry. (B) Diffuse reflectance spectra of the materials investigated in this study: MIL-125(Ti) (grey), NH₂-MIL-125(Ti) (orange) and MR-MIL-125(Ti) (red). (C) Photocatalytic benzaldehyde evolution. No catalyst (grey), NH₂-MIL-125(Ti) (orange) and MR-MIL-125(Ti) (red). 200 μ L of benzyl alcohol/12 mL CH₃CN and 150 W Xe lamp. 12 mg of NH₂-MIL-125(Ti) and 18 mg of MR-MIL-125(Ti). Reprinted with permission from ref. 185. Copyright 2013, The Royal Society of Chemistry.

increasing the ratio of BDC-NH₂ and BDC (10%, 50%, and 100% BDC-NH₂, which are equal to 1, 6, and 12 BDC-NH₂ linkers per unit cell), the molar extinction coefficient notably has a proportionate increase with the -NH₂ substituted linker content. To further explore the donating characteristics of aromatic amines, a mixture of 10% diaminated BDC-(NH₂)₂ and 90% BDC-NH₂ was constructed to study its band structure. The band gap decreases to 1.28 eV with the rational selection of the substituent of the diaminated BDC linker (Fig. 13A). Finally, the introduction of 10% BDC-R (R represents -OH, -CH₃, and -Cl) reconfirmed that the substitution of the electron donating group on the phenyl ring can lower the optical band gap.

Besides purposely synthesizing Ti-MOFs through choosing suitable Ti precursors and organic linkers, post-synthetic modification (PSM) can also be an alternative way for MOF design. After the as-prepared NH₂-MIL-125 reacted with nitrosonium ions and then reacted with diethylaniline, red-MIL-125 (MR-MIL-125) containing methyl red-like organic dye was prepared to improve the optical absorption.¹⁸⁵ The calculated optical band gap of MR-MIL-125 was \sim 1.93 eV. Photoconductivity measurements demonstrated that the properties of MIL-125 could be judged as an array of self-assembled molecular catalysts rather than classical semiconductors because the poor photoconductance kept the electrons in a localized state, whereas 30% content of MR-functionalized in this red-MIL-125 could enhance 40% contribution in activity. Due to the extended conjugation of the aromatic system, there is a clear red shift of the absorption edge to almost 700 nm (Fig. 13B and C).

Logan *et al.* reported a series of Ti-MOFs isorecticular to NH₂-MIL-125 by tailoring *N*-alkyl amino groups.¹⁸⁶ As a consequence of the polarization of a chemical species in electronegativity between a heteroatom and carbon atoms in the alkyl chains,

varying the length and connectivity of the decorated alkyl chain in close proximity to the amino group could increase electron density and destabilize the top of the VB to result in a narrower band gap. A progressive decrease in the surface area and pore volume was observed, which was induced by *N*-alkyl substitution in the N₂ gas absorption and CO₂ adsorption isotherms. Among these series, the *n*-heptyl substituted counterpart exhibited a higher band gap than the cyclohexyl analogue, close to that of the *n*-butyl substituted counterpart, which can be attributed to the inductive effects decreasing with the increasing distance between the heteroatom and C-C σ -bond. Except that, stronger electronic induction can be achieved by the σ -bonds of cyclic substituents consistent with the increased electron density.

In addition to amino functionalization, small variations of organic linkers or metal ions can also enhance the photocatalytic performance. Li and co-workers have prepared Ti-substituted NH₂-UiO-66, in which Ti atoms make substantial contribution to the bottom of the CB of this mixed-metal MOF.¹⁸⁷ The substituent Ti moiety can act as an electron mediator in promoting the electron transfer, resulting in a longer lifetime of the charge-separated state, where the Ti-substituted NH₂-UiO-66 exhibits a broader light absorption spectrum with a shoulder peak extending to 500 nm compared to NH₂-UiO-66. A lack of crystalline collapse and the presence of peaks corresponding to other Ti species ruled out the possibility of the formation of Ti-based impurities. Subsequently, Lee *et al.* further developed 1(Zr/Ti) by mixed-ligand and mixed-metal modification *via* post-synthetic exchange (PSE), and the inductively coupled plasma mass spectroscopy (ICP-MS) and BET data supported the argument that Ti was substituted for Zr in MOF SBUs. PL measurement provided the evidence for charge transfer in 1(Zr/Ti), and the remarkably reduced emission intensity compared to the original structure indicated the efficient charge transfer of photogenerated electrons by LMCT. In addition, the energy band structure revealed that 1(Zr/Ti) has two light absorption routes, which can exactly broaden the light absorption coverage of the MOF (Fig. 14A and B).¹⁸⁸ This study suggests a novel way to obtain additional light absorption by linker modification and metal incorporation.

To have a deep insight into the metal doping strategy, Gason and co-workers clearly elucidated that Ti was incorporated in the linker vacancy sites *via* metal appendage rather than the replacement of Zr in the SBUs of UiO-type materials, giving researchers a glimpse of this engineering for metal incorporation.¹⁸⁹ Inspired by those studies, Belver and co-workers prepared new mixed Ti-Zr MOFs based on NH₂-MIL-125 with different Ti : Zr ratios and clearly elucidated that the amount of Zr incorporated in NH₂-MIL-125 can influence the crystallinity.¹⁹⁰ Within a certain scope of the doped Zr amount, the structural integrity of this mixed-metal NH₂-MIL-125 remains unchanged. When the amount of doped Zr exceeded the threshold, mixed-metal NH₂-MIL-125 with an amorphous structure and lower porosity was obtained. By choosing an appropriate Ti content, the mixed Ti-Zr MOF shows a high surface area, essentially a microporous texture and lower charge recombination rate featuring better photoactivity.

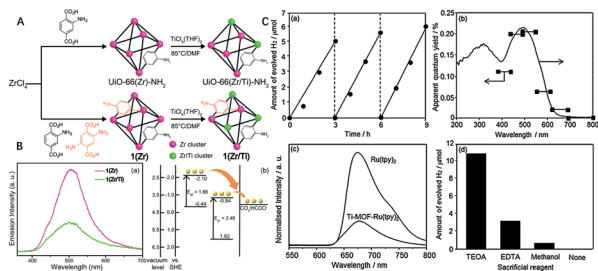


Fig. 14 (A) Synthesis of a mixed-ligand MOF 1(Zr) *via* PSE to obtain mixed-metal MOFs 1(Zr/Ti) and UiO-66(Zr/Ti)-NH₂. (B) (a) Photoluminescence spectra of both 1(Zr) and 1(Zr/Ti). (b) Energy band structure of 1(Zr/Ti) derived from UPS and F(R) results. Heterogeneous ligands formed two energy levels in the MOF, which potentially catalyze CO₂. Reprinted with permission from ref. 188. Copyright 2015, The Royal Society of Chemistry (C). (a) Time course of photocatalytic hydrogen production under visible-light irradiation ($\lambda > 420$ nm) from water containing 0.01 M TEOA and 0.05 mM H₂PtCl₆ using Ti-MOF-Ru(tpy)₂ for a total of 9 h with intermittent evacuation and exposure to atmospheric conditions every 3 h. (b) Wavelength-dependent apparent quantum efficiency for the hydrogen evolution reaction from water containing 0.01 M TEOA and 0.05 mM H₂PtCl₆ using Ti-MOF-Ru(tpy)₂. (C) Photoluminescence spectra of Ti-MOF-Ru(tpy)₂ and Ru(tpy)₂ measured under vacuum at 77 K (excitation: $\lambda_{\text{ex}} = 520$ nm). (d) Sacrificial reagent dependence of photocatalytic hydrogen production under visible-light irradiation ($\lambda > 420$ nm) over Ti-MOF-Ru(tpy)₂ for a reaction time of 6 h. Reprinted with permission from ref. 197. Copyright 2014, The Royal Society of Chemistry.

Owing to their high light sensitivity, molecular dyes can be implemented as the ligands through the direct synthesis of the envisaged scaffold or by PSM.^{191–195} Pullen *et al.* firstly immobilized an iron complex [FeFe]-(dcbdt)(CO)₆ as a proton reduction catalyst on the framework of UiO-66.¹⁹⁶ Taking advantage of the labile bonds between the Fe centres and the electron-deficient H₄dcbdt linker, this complex can be homogeneously incorporated into UiO-66 with a modest decrease in pore size distribution. The incorporation of this iron complex can even prevent reduced species from non-productive charge recombination. Besides, optimizing the PSE conditions can elevate the photocatalytic performance of the diiron-catalyst-incorporated MOF in contrast to the homogeneous counterpart. Following this strategy, Toyao *et al.* reported the incorporation of a Ru complex (Ru(bpy)₂) with a broader absorption spectrum and lower highest occupied molecular orbital (HOMO) level than those of BDC-NH₂ into the typical MOF NH₂-MIL-125.¹⁹⁷ The interpenetration of this Ru complex enormously decreased the surface area and pore size, and the results showed that the trend of the apparent quantum efficiency matches well with that of the extended absorption spectrum, demonstrating superior photocatalytic ability in accordance with better light harvesting behaviour (Fig. 14C). Last but not least, the lower luminescence intensity of Ti-MOF-Ru(tpy)₂ compared to pure Ru(tpy)₂ suggested that efficient charge transfer occurred from the dye molecule to the Ti-oxo cluster.

As for designable surface potentials and tunable mass-transfer ability of MOFs, a number of studies based on exploiting their immobilization and stabilization at the

nanoscale have been explored in a reproducible and reliable manner. The encapsulation of MNPs in MOF pores can facilitate the charge migration, resulting in a longer lifetime of the charge-separated state.^{198,199} Encapsulating surface plasmon resonance (SPR) active species (*i.e.* Pt, Pd, and Au) in the spatial confinement of the Ti-MOF cavities could also achieve a remarkable performance of photocatalysis.

In the case of amino functionalization, attractive modification ways for better photocatalytic activity included mixed ligands/metal modification, metal doping and photo-sensitization of Ti-MOFs with dye molecules, and the cooperative action between the typical characteristics of MOFs with the catalytic nature of guest species in the pore/cage/channel for synergistic catalysis.²⁰⁰ Recently, with the in-depth exploration of polymers, metallic complexes, metal oxides and graphitic carbon nitride (g-C₃N₄), the organization of the guest series loaded in Ti-MOFs with a spatially defined manner has the potential to enable synergistic functions for solar energy utilization, which will be discussed below.

4.2 Photocatalytic water splitting

Hydrogen, an attractive energy carrier, can store solar energy in its chemical bond, which can be released through direct combustion with only water as the by-product. There are many efforts in using a heterogeneous photocatalyst for large-scale H₂ production *via* artificial photosynthesis.^{201–205}

MIL-125 possessed a large band gap of 3.60 eV, which can only absorb UV light. Under UV irradiation, MIL-125 with alcohols in its cavities clearly changed its color from white to purple-gray-blue within a few seconds under inert gas (nitrogen), which is reversible upon exposure to O₂. The phenomenon was explained by the intervalence electron transfer hopping in MIL-125, and the conversion between Ti(III) and Ti(IV) proven by EPR spectra. However, further investigation triggered by this photochromic phenomenon was instantly blocked by the large band gap of MIL-125. NH₂-MIL-125, as an analogue of MIL-125 with amine functionalization, was reported to be utilized for visible-light-driven photocatalytic hydrogen evolution by Matsuoka's group, as shown in Fig. 15.²⁰⁶ Since the bandgap of NH₂-MIL-125 (2.60 eV) became lower than that of MIL-125 (3.60 eV), visible light can be used to irradiate it. After irradiation, an electron from the amino group transfers to the Ti-oxo cluster, which promotes the conversion of Ti⁴⁺ to Ti³⁺. With the existence of the co-catalyst Pt, NH₂-MIL-125 has a good photocatalytic H₂ evolution performance, and H₂ production reaches 17 $\mu\text{mol g}^{-1} \text{h}^{-1}$, exhibiting superior photoactivity compared to UiO-66 type MOFs. PXRD of the sample disposed with intermittent evacuation and exposure to air conditions indicated the integrity of NH₂-MIL-125.

A facile approach for the encapsulation of Au, Pt and Pd nanoparticles into MIL-125 without any extra reducing or stabilizing agents was promising to prepare high-quality metal MNPs/MOFs.²⁰⁷ HRTEM images clearly show the characteristic lattice fringes of the MNPs and no obvious agglomeration of the initially formed small MNPs. It's worth noting that Pt/MIL-125

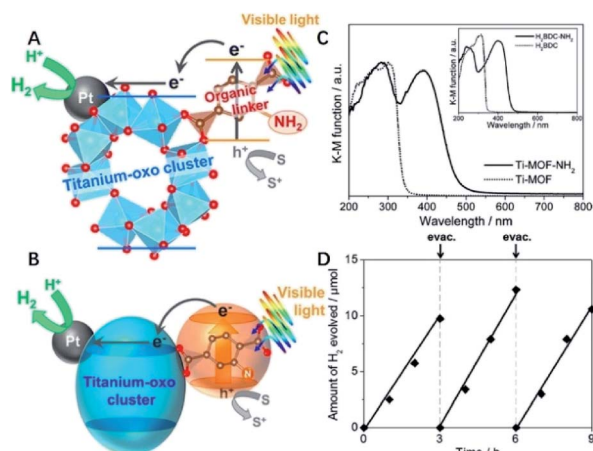


Fig. 15 (A and B) Schematic illustration of a photocatalytic hydrogen production reaction over Pt-supported Ti-MOF-NH₂ on the basis of the LCCCT mechanism. (C) DRUV-vis spectra of Ti-MOF (dotted line) and Ti-MOF-NH₂ (solid line). Inset shows the DRUV-vis spectra of H₂BDC (dotted line) and H₂BDC-NH₂ (solid line). (D) Time course of photocatalytic hydrogen production under visible-light irradiation ($\lambda > 420$ nm) over Pt/Ti-MOF-NH₂ for a total of 9 h with intermittent evacuation and exposure to atmospheric conditions every 3 h. Adapted with permission from ref. 206. Copyright 2012, American Chemical Society.

through a Ti³⁺-assisted method exhibited superior H₂ evolution activity in contrast to analogous counterparts prepared by a direct photodeposition method. The corresponding turnover number (TON) based on the Pt amount is 30.2, which is an 80% increase relative to the traditional way. However, there is no discussion about the stability and recyclability of this heterogeneous photocatalyst.

The appropriate size and distribution of the MNPs encapsulated in the Ti-MOF can promote the performance of H₂ evolution under light irradiation by synergistic effects, originating from the Ti-MOF framework and the SPR effect of MNPs. Notably, by optimizing the amount of the hole scavenger (CH₃OH) in the UV photo-assisted deposition of Pd, appropriate control of the size and location of Pd can be achieved. The Pd/NH₂-MIL-125 (ref. 208) heterogeneous composite can generate hydrogen at a linear rate after the initial period for the dehydrogenation of formic acid (a useful hydrogen storage material). This result is higher than that of the analogue counterparts, which is attributed to the basic functionalization of NH₂-MIL-125 and small Pd NP size.²⁰⁹ Researchers may draw insights from this work for in-depth understanding of H₂ evolution in water splitting by metal doping in Ti-MOFs.

Illuminated by the plasmonic efforts and Schottky junctions, a Pt@MOF/Au catalyst with two types of metals was designed to show two orders of magnitude activity enhancement of the hydrogen evolution rate (1743.0 $\mu\text{mol g}^{-1} \text{h}^{-1}$) in reference to other control groups under light irradiation (Fig. 16).²¹⁰ PXRD profiles and TEM images confirmed the homogeneity of this composite after reaction, and the strong Ti³⁺ signal was attributed to the greatly accelerated electron charge transfer. The

composite was used for three runs showing no significant decrease in photoactivity. Notably, the plasmonic efforts of Au nanorods and the Pt-MOF Schottky junction synergistically boost the photocatalytic ability of MIL-125, by elaborately steering the formation of the charge flow and expediting the charge migration, which may provide more opportunity toward more efficient solar energy valorization in future endeavour.

The insertion of photoactive molecules into the cavities of MOFs to form a guest@MOF system is an efficient way to improve the activity of MOF photocatalysts. The oxygen-tolerant cobaloxime complex was loaded into the pores of NH₂-MIL-125 by the PSM approach (Ship-in-a-Bottle technique).²¹¹ Co@NH₂-MIL-125 exhibited a 20-fold enhancement in hydrogen evolution under visible-light illumination compared to NH₂-MIL-125 (Fig. 17). No leaching of the Co complex occurs in the Co@NH₂-MIL-125 composite. Also, the recycling experiments showed that there was almost no loss of activity after about 70 h of illumination, indicating the high stability of this composite. EPR measurements confirmed that Co was the active site for H₂ generation. Under light illumination, the MOF backbone absorbs light and transfers electrons to the cobalt species within the composite, which then reduces H⁺ to H₂. It can be confirmed that the Co complex over the bulk of the MOF matrix is highly dispersed.

Following the strategy of cooperative effects which combine a photoactive matrix and catalytically active encapsulated guest, another Co(II) complex ([Co^{II}(TPA)Cl][Cl] (TPA = tris(2-pyridylmethyl)amine)) was loaded into the pores of NH₂-MIL-125, which reached a high H₂ production rate (553 $\mu\text{mol g}^{-1} \text{h}^{-1}$) as compared to NH₂-MIL-125 (17 $\mu\text{mol g}^{-1} \text{h}^{-1}$).²¹² Furthermore, the Co(II)@MOF composite is nearly identical to the virgin NH₂-MIL-125 with no agglomerates or core/shell type structure, as evidenced by HRTEM. The stability of this composite was confirmed by determining the absence of Co leaching and the

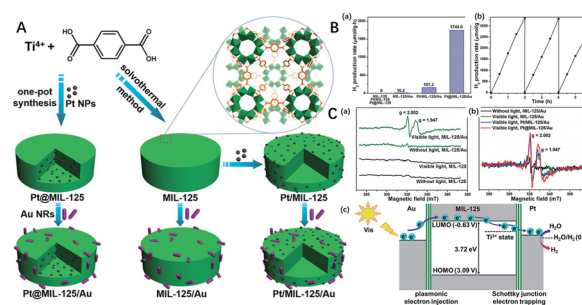


Fig. 16 (A) Schematic illustration showing the synthesis of Pt@MIL-125/Au and the corresponding Pt/MIL-125/Au and MIL-125/Au analogues. (B) (a) Photocatalytic H₂ production rates of different catalysts. (b) Recycling performance of Pt@MIL-125/Au. The reaction with the photocatalyst (5 mg) in MeCN/TEOA/H₂O (9 : 1 : 0.15 v/v/v, 20 mL) under the irradiation of 380–800 nm light with a 300 W Xe lamp (LX-300F, Japan). (C) ESR spectra of (a) MIL-125 and MIL-125/Au, and (b) MIL-125/Au, Pt/MIL-125/Au, and Pt@MIL-125/Au at 140 K in the absence or presence of visible-light irradiation for 300 s. (c) Schematic illustration showing the electron migration at the two metal-MOF interfaces based on the energy levels. Reprinted with permission from ref. 210. Copyright 2018, WILEY-VCH Verlag GmbH.

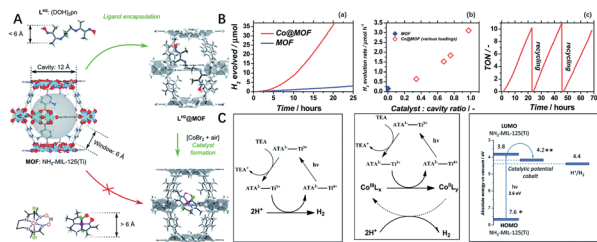


Fig. 17 (A) 'Ship-in-a-bottle' synthetic strategy followed for the assembly of Co@MOF. (B) (a) Photocatalytic proton reduction using the MOF and Co@MOF. (b) Steady state H₂ evolution rate plotted against the average number of cobalt atoms inside each MOF cavity. (c) Recycling tests on Co@MOF bearing medium cobalt loading. Conditions: 5 mg catalyst, 5 mL CH₃CN, 1 mL TEA, 0.1 mL H₂O, and 500 W Xe/Hg lamp using $\lambda > 408$ nm. (C) Proposed hydrogen evolution mechanisms in the pristine MOF (left) and Co@MOF (centre). ATA = 2-aminoterephthalic acid. Schematic diagram of redox potentials of components of the Co@MOF composite (right). (*): calculated values. (**): experimental data. Concept of photocatalytic H₂ production using a Co@MOF-125 composite. Adapted with permission from ref. 211. Copyright 2015, The Royal Society of Chemistry.

reusability of Co(II)@NH₂-MIL-125 several times without the loss of photoactivity. This guest@MOF composite also facilitates the photoinduced charge transfer from the MOF to the Co(II) complex, which can greatly improve the spatial charge separation, thus significantly improving the photocatalytic activity of H₂ evolution.

An ionic nickel(II) species ([Ni(dmobpy)(2-mpy)₂] (dmobpy = 4,4'-dimethoxy-2,2'-bipyridine, 2-mpy = 2-mercaptopyridyl)) was loaded into NH₂-MIL-125 by stepwise assembly of the complex in the presence of the MOF to form a new Ni@NH₂-MIL-125 composite.²¹³ Under UV-light irradiation, the composite demonstrated a high TOF of 28 mol g(Ni)⁻¹ h⁻¹ for H₂ generation under improved conditions. Mechanically mixed NH₂-MIL-125 and Ni(II) complexes as well as solid Ni(NO₃)₂·6H₂O and pristine MOF were used to figure out the origin of Ni species responsible for this photocatalysis. The results elucidated that two different Ni species account for the efficient photocatalytic performance of this hybrid composite, whereas, the well-retained structural integrity of this composite which is associated with the original MOF itself after the loop test is not figured out. Those Ti-MOFs in work can be an ideal scaffold for the heterogenization of homogeneous complexes.

A post-solvothermal route for the outer-to-inner loss of organic linkers from Ti-MOF was operated at low temperature compared to the commonly adopted pyrolysis method. This NH₂-MIL-125@TiO₂ core-shell particles provide a void space and a mesoporous structure,²¹⁴ which can provide more active sites and facilitate mass/charge transfer. Remarkably, NH₂-MIL-125@TiO₂ exhibited a high hydrogen generation rate of 496 μmol g⁻¹ h⁻¹, which is 70 times higher than that of the raw materials and exceeds the photoactivities of noble-metal-loaded MOF catalysts. In addition, this core-shell architecture retained its integrity up to three runs and prevented the agglomeration of particles.

The fabrication of hierarchical porous Ti-MOF/COF hybrid materials was synthesized by the reaction between NH₂-MIL-125 and benzoic-acid-modified covalent triazine-based frameworks (B-CTF-1) *via* covalent bonds instead of the traditional combination modes through van der Waals forces or hydrogen bonds.²¹⁵ The hydrogen generation (360 μmol g⁻¹ h⁻¹) over the optimized Ti-MOF/COF composite is 2.2 and 2.1 times that of the original CTF-1 and benzoic acid-functionalized CTF-1 nanosheets, and the superior hydrogen evolution performance of this material was ascribed to the formation of amide bonds between COFs and MOFs, resulting in the efficient separation of electron-hole pairs. To further validate this innovative strategy, a similar postsynthetic covalent modification between NH₂-UiO-66 and CTF-1 was also achieved with typical photocatalytic performance, in accordance with empirical expectation. In addition, NH₂-UiO-66/B-CTF-1 showed better photocatalytic performance compared to NH₂-MIL-125/B-CTF-1 obtained from the formation of polar amide covalent bonds between the COF and MOF.

g-C₃N₄ has been investigated in various photocatalytic applications as a metal-free polymeric semiconductor due to its excellent physiochemical properties and flexible layered structure, which can anchor and wrap onto Ti-MOFs with an intimate contact beneficial to interfacial electron transfer. Thus, Xu *et al.* reported a novel NH₂-MIL-125/g-C₃N₄ heterostructure decorated with NiPd co-catalysts for efficient photocatalytic hydrogen production.²¹⁶ With different ratios of MNPs, excellent hydrogen evolution performance of this as-fabricated heterostructural photocatalyst was achieved which is 322 times higher than that of NH₂-MIL-125/g-C₃N₄. The role of NH₂-MIL-125 in the contribution of hydrogen generation performance can be ascribed to three main aspects: (1) the large intimate contact interface between NH₂-MIL-125 and g-C₃N₄ is suitable for the uniform distribution of NiPd NPs. (2) The porous NH₂-MIL-125 can promote the mass/charge transfer favouring the separation of electron-hole pairs. (3) NH₂-MIL-125 acting as a photoelectron incubator can enhance the photoactivity of hydrogen generation.

Given that the Z-scheme concept was proposed to maximize the redox potential of the heterojunction system,²¹⁷ a novel Z-scheme heterostructured catalyst (termed CFBM) consisting of NH₂-MIL-125 and g-C₃N₄ functionalized by benzoic acid (CFB) *via* covalent bonds was prepared to elevate photocatalytic performance (Fig. 18).²¹⁸ With the increase of the amount of CFB coating on g-C₃N₄/NH₂-MIL-125, the hydrogen production rate was enhanced in good agreement with the improved results of PL and electrochemical impedance spectroscopy (EIS) measurements. After four cycles, this hybrid covalently bonded composite with high stability and a long-life charge separation state exhibited better photoactivity than conventional heterostructured catalysts through van der Waals force. In this heterostructure, benzoic acid can act as an electron mediator to efficiently separate photogenerated electrons and holes. Meanwhile, the photogenerated electrons of BDC-NH₂ can be transferred to Ti-oxo clusters *via* LMCT, leading to the formation of Ti³⁺, which is beneficial for hydrogen production.

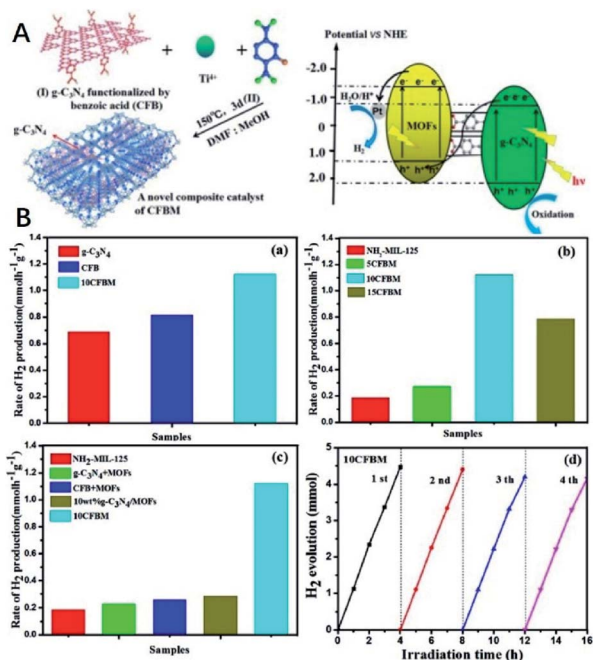


Fig. 18 (A) Schematic representation of the synthesis of covalently linked CFMB composites. (I) g-C₃N₄ functionalized with benzoic acid (CFB) and (II) *in situ* growth of CFMB crystals. Photocatalytic mechanism of the charge transfer for hydrogen evolution over 10CFBM under visible light irradiation. (B) PL spectra of the as-prepared catalysts at an excitation wavelength of 325 nm (a); electrochemical impedance spectra of the as-prepared catalysts (b). (c) The rate of hydrogen evolution over the different samples under visible light irradiation (a–c). (d) The cycling runs of the 10CFBM catalyst under visible light irradiation for 16 h. Reprinted with permission from ref. 217. Copyright 2018, Elsevier B.V.

The doping of Ir- and Ru-complex-derived dicarboxylate ligands into the Ti₃-BPDC framework was applied in visible light-driven photocatalytic hydrogen evolution.¹⁵¹ ICP-MS analysis revealed that the Ti/Ir ratio of Ti₃-BPDC-Ir is 3.25 and the Ti/Ru ratio of Ti₃-BPDC-Ru is 4.82, respectively. The TONs of Ti₃-BPDC-Ir and Ti₃-BPDC-Ru reached 6632 and 786 after 72 h under visible light irradiation, in contrast to the modest TONs of a mechanical mixture of the Ti₆O₆ cluster and Ir complex or Ru complex. Additionally, the mechanism of energy transfer in the reaction between photosensitizers and Ti-oxo clusters was clearly studied, which was confirmed *via* photophysical, electrochemical and DFT studies.

4.3 Photocatalytic CO₂ reduction

The accumulation of CO₂ is one of the hottest disputed issue in the global warming, so the fixation of a large amount of carbon dioxide creating a useable feedstock of reduced carbon artificial photosynthesis has triggered lots of studies.^{85,219–223}

In 2012, Li and co-workers used NH₂-MIL-125 to reduce CO₂ to HCOO[−] under visible-light illumination in the presence of triethanolamine (TEOA) as a sacrificial agent and acetonitrile as the solvent, which is the first endeavour of Ti-MOFs.¹⁵⁶ The formation of formate can be detected in the resulting products with an amount of 8.14 μmol in 10 h. The NH₂ group in NH₂-

MIL-125 is quite essential for photocatalytic CO₂ reduction. The reaction mechanism for photocatalytic CO₂ reduction is proposed, as shown in Fig. 19. Upon the illumination of visible light, the amine-functionalized ligands transfer electrons to Ti⁴⁺ to form Ti³⁺ *via* a LMCT process. Then, Ti³⁺ reduces CO₂ to HCOO[−], whereas TEOA acts as an electron donor.

An isorecticular series of Ti-based NH₂-MIL-125 to reduce CO₂ under blue irradiation were reported.¹⁸⁶ In this series, most of the *N*-alkyl substitutions in MIL-125-NHR (where R = methyl, ethyl, isopropyl, *n*-butyl, cyclopentyl, cyclohexyl, and *n*-heptyl) showed higher CO₂ conversion compared to NH₂-MIL-125 (Fig. 20). Their study revealed that secondary *N*-alkyls, isopropyl, cyclopentyl, and cyclohexyl (Fig. 20c blue histograms) display a larger quantum yield (1.5–1.8%) than the primary *N*-alkyls (0.30–0.40%, Fig. 20c orange histograms). Among them, MIL-125-NHCyp demonstrated the largest apparent quantum yield (1.80%), which is almost 6 times the quantum yield of NH₂-MIL-125. Considering that there is no correlation between the photocatalytic efficiency and gas absorption ability, the increased photocatalytic activity of secondary alkyl substituent species coincides with the decreased bandgap and increased excited-state lifetime. All MOFs showed good photochemical stability after reuse.

To achieve cooperative action of a high specific surface area and excellent ultraviolet absorption ability, a high ordered hierarchical macroporous MIL-125 structure, which combines

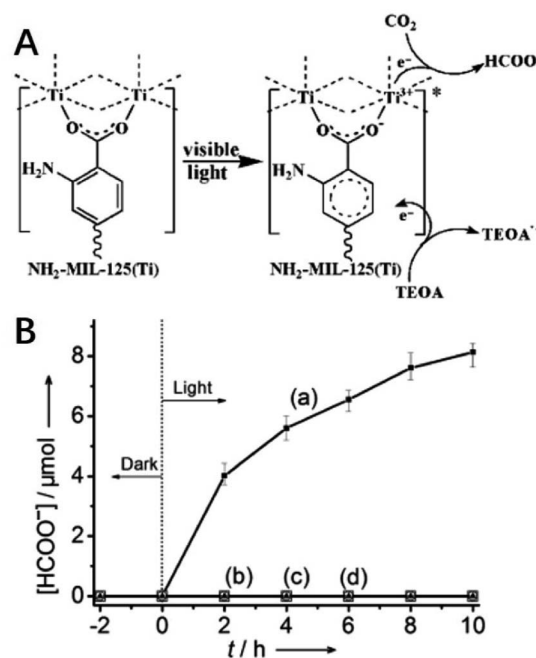


Fig. 19 (A) Proposed mechanism for photocatalytic CO₂ reduction over NH₂-MIL-125(Ti) under visible light irradiation. (B) The amount of HCOO[−] produced as a function of the time of irradiation over (a) NH₂-MIL-125(Ti) (■), (b) MIL-125(Ti) (□), and (c) a mixture of TiO₂ and H₂ATA (19 mg + 32 mg) (○), and (d) visible light irradiation without a sample (▲). The solutions were irradiated using a Xe lamp with filters producing light in the range of 420–800 nm. Photocatalysts: 50 mg, MeCN/TEOA (5 : 1), and solution volume: 60 mL. Adapted with permission from ref. 156. Copyright 2012, WILEY-VCH Verlag GmbH.

To investigate the mechanism of photocatalytic oxidation of benzyl alcohol to benzaldehyde by DGIST-1, which displayed >99.5% selectivity, a high conversion (93%) and appreciable turnover number ($190 \mu\text{mol mg}^{-1}$) in the absence of cocatalysts, DMPO was used as a superoxide species scavenger while TMP as a singlet oxygen species scavenger or in the presence of phenol as a hole scavenger.¹⁴² The yield of benzyl alcohol oxidation with any scavenger was dramatically decreased, and this controlled experiment elucidated the pivotal role of holes, superoxide species and singlet oxygen in the oxidation of benzyl alcohol. Intriguingly, the twice recycled DGIST-1 exhibited typical stability, reconfirming that porphyrin Ti-MOFs can be efficient photocatalysts in the selective oxidation of alcohols to aldehydes.

Pt/NH₂-MIL-125 has been studied in the photocatalytic reduction of nitrobenzene to nitrosobenzene and aniline under visible light irradiation.²²⁵ Later, the substrate scope for the aerobic oxidation of amines over NH₂-MIL-125 was investigated.²²⁶ Acetonitrile was found to be the optimum medium among all the solvents tested, and the different substituents on the phenyl ring can alter the conversion rate and selectivity resulted from the existence of the electronic effect. Amines bearing electron withdrawing substituents on the phenyl ring decreased selectivity and conversion. The reaction rate in the order of *para*- < *meta*- < *ortho*-substituted results from the steric hindrance of methoxy substituted at different positions of the phenyl ring of benzylamine, and there is no oxidation occurring for amine lacking hydrogen at the α -carbon, indicating the crucial role of α -H in the catalysis. The enhanced performance was also reconfirmed by the reaction carried out without using a cut-off filter.

An electron-conduction bridge was constructed from Ag NPs photodeposited on the surface of g-C₃N₄ and MIL-125, facilitating the direct migration of photoinduced electrons from g-C₃N₄ to MIL-125 and retarding the combination of electron-hole pairs.²²⁷ When the content of g-C₃N₄ was controlled at an optimal value, the oxidation of various aromatic alcohols to the corresponding carbonyl compounds revealed that alcohol compounds with electron-donating substituents can enhance the photocatalytic activity, while lower yields of alcohol substituted by electron-withdrawing groups were observed, which is even prevalent in the case of benzhydrol systems. The results of the photocatalytic reduction of various aromatic nitro compounds with electron effects are contradictory to the observation of the oxidation of aromatic alcohols. Electron-withdrawing groups substituted in the nitro compounds are beneficial for photocatalytic reduction performance. The photoreduction of nitro compounds and oxidation of the alcohols with superior conversion and selectivity not only indicate the feasibility of this heterostructured nanocomposite, but also show the increase of the electron-donating ability of the corresponding substituent group in alcohols corresponding to the conversion capability.

To develop efficient catalysts for the cleavage of the N \equiv N bond, which is a kinetically challenging process,^{228,229} a series of isorecticular NH₂-MIL-125 were harnessed to undergo photocatalytic nitrogen fixation to form NH₃ under visible-light irradiation without any sacrificial agent.²³⁰ All the analogous MOFs

with functionalized ligands were photoactive for N₂ fixation, while the amino-functionalized NH₂-MIL-125 exhibits the highest visible light efficiency at a rate of $12.3 \mu\text{mol g}^{-1} \text{h}^{-1}$ compared to -OH and -CH₃ substituted counterparts (Fig. 22). The different photocatalytic response properties are likely originated from the electronic structure where the strong electron-donating characteristics of aromatic functional groups can lead to reduction of the band gap consistent with the simulated studies. PL and ESR measurements can prove that N₂ was firstly captured by the Ti₈O₈ clusters with defect sites, and then underwent reduction to ammonia assisted by Ti³⁺ sites in the presence of water as an electron donor. The high reaction rate of NH₂-MIL-125 can be rationalized with the increase of the light absorption spectrum and higher exchange ratio to induce more Ti³⁺ which is beneficial to the reduction of nitrogen.

Isorecticular Ti-MOFs (MOF-901 and MOF-902) were investigated for the photocatalytic polymerization of various monomers, such as methyl methacrylate (MMA), benzyl methacrylate (BMA), and styrene under visible light irradiation.¹⁵⁴ Polymers with a high yield, high molecular weight, low polydispersity index and uniform distribution were prepared. Taking advantage of the longer conjugated linker units, MOF-902 exhibited better photocatalytic performance in contrast to MOF-901 possessing a higher band gap. Stability and recyclability can be confirmed by the unchanged crystal structure and BET surface area after three consecutive cycles.

Ti-TBP was synthesized as a photocatalyst in hypoxia-tolerant type I photodynamic therapy (PDT).¹⁵⁸ Upon light irradiation, Ti-TBP not only transfers electrons from excited ligands to the Ti-oxo cluster, but also sensitizes singlet oxygen production. Ti-TBP as a photocatalyst leads to an efficient tumor regression of 98.4% in volume with a cure rate of 60%, in

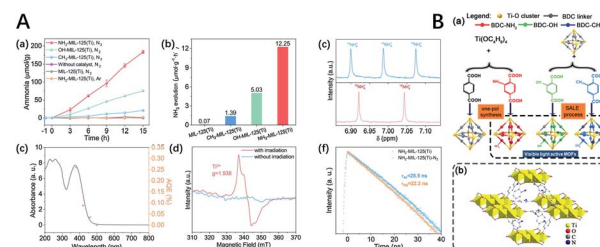


Fig. 22 (A) (a) The amount of NH₄⁺ produced as a function of irradiation time over NH₂-MIL-125(Ti), OH-MIL-125(Ti), CH₃-MIL-125(Ti), MIL-125(Ti), no catalysts, and NH₂-MIL-125(Ti) with Ar pumping. Conditions: photocatalysts, 25 mg; water solution, 100 mL; visible light (400–800 nm). (b) Production yield rates of ammonia over photocatalysts for 15 h. (c) 1H NMR spectra of the products *via* reaction over photocatalysts in different reaction atmospheres. (d) Wavelength-dependent apparent quantum efficiency of NH₂-MIL-125(Ti) under monochromatic light irradiation. (e) Low-temperature ESR spectra of the as-prepared NH₂-MIL-125(Ti) before and after light irradiation. (f) The time-resolved photoluminescence decay curves of NH₂-MIL-125(Ti) under Ar and N₂ atmospheres. (B) (a) Schematic diagram of the targeted visible light active MOFs for photocatalytic N₂ fixation. (b) Schematic drawing of the structure of NH₂-MIL-125(Ti). Perforated cyclic octamer with edge- and corner-sharing TiO₅(OH) octahedra (yellow part); N of the free amino groups (blue dots). Reprinted with permission from ref. 230. Copyright 2020, Elsevier B.V.

excess of the tumor inhibition performance over the corresponding Hf counterpart and homogeneous control, and the nontoxic nature of Ti-TBP-mediated PDT treatment was confirmed by no difference in behaviour and organ function after treatment.

With the modification of Ag NPs dispersed on the surface of MIL-125 microspheres,²³¹ (the amount of Ag loaded as a co-catalyst was determined to be 3 wt%), this composite (Ag(3 wt%) @MIL-125) almost completely degraded all rhodamine B (RhB) under light illumination. However, although MIL-125 also displayed a typical photocatalytic activity for the visible-light-induced degradation of RhB, its degradation rate for RhB is only about 8% after 40 min of visible light irradiation. The photocatalytic activity of this composite is four times higher than that of P25 TiO₂, which is used as a benchmark photocatalyst. Also, this hybrid composite can be reused at least five times without significant loss of photocatalytic performance.

NTU-9 exhibited an excellent performance for dye degradation under visible light irradiation ($\lambda > 420$ nm).¹⁴⁴ With the existence of NTU-9, RhB and methylene blue (MB) in aqueous solution were degraded completely after 80 min and 20 min, respectively. After 6 h of the dye degradation experiment, NTU-9 still retained the excellent photocatalytic performance and the integral crystal structure. The incorporation of other semiconductors into MOFs to form a heterojunction is an efficient approach to improve the photocatalytic activity of MOFs. Novel metal nanoparticles,^{207,232} r-GO,²³³ In₂S₃,²³⁴ g-C₃N₄,^{235,236} Ag₃PO₄,²³⁷ CdTe²³⁸ and BiOI²³⁹ were used to form heterostructures, which all showed enhanced photocatalytic dye degradation efficiency.

Besides photocatalytic applications, Ti-MOF also showed promising applications in gas storage and separation,^{240–245} chemical sensors,^{246–248} optoelectronics,^{249–252} solar cells²⁵³ and other applications.^{254–259} Due to the length limit of this review, these topics will not be covered here.

5. Conclusion and outlook

The development of Ti-based MOFs is still in its infancy. Till now, only limited Ti-MOF structures have been reported; especially the number of Ti-MOFs based on infinite Ti-oxo chains and sheets is small. Most of the new Ti-MOF structures were reported after 2014 when new architectural design and synthesis strategies were employed. In the case of the diversity of Ti-oxo clusters, we believe that there should be more new structures emerging in the next few years.

In this review, we summarized the recent progress of Ti-MOFs. The different synthesis conditions such as solvents, temperature, reaction time, Ti precursors, modulator and the Ti/ligand ratio can lead to new Ti-MOFs. We also discussed the photocatalytic activity of these Ti-MOFs including photocatalytic alcohol oxidation, photocatalytic H₂ generation, photocatalytic reduction of CO₂ and photocatalytic dye degradation. We believe that such discussions could encourage scientists to become involved in the research field of Ti-MOFs.

However, the synthesis and applications of new Ti-MOF materials are still very challenging. The synthetic conditions of

Ti-MOFs are still case-by-case based, and there is still no general method to prepare new Ti-MOFs. The addition of modulators such as acetic acid or benzoic acid, which has been widely utilized in the synthesis of Zr-based MOFs, may be a good resolution. In fact, this strategy has been successfully used in the preparation of high-quality single crystals of Ti-MOFs (PCN-22) with benzoic acid as the modulator. Clearly, this method might be extended to prepare other Ti-MOFs. In addition to direct synthesis, Ti-MOFs can be obtained by the usage of mixed metal and/or mixed linkers, or by a metal- or linker-exchange method. With rational elaboration design, the combination of open metal sites and functional groups can make Ti-MOFs a suitable scaffold for synergistic catalysis, which is difficult to achieve in homogeneous catalysis. Although there are thousands of organic ligands that can be combined with metal ions to form MOFs, only limited organic ligands could coordinate with Ti to form crystalline MOFs. Ti-MOFs containing N-ligands have not been reported to date. Like TiO₂, Ti-oxo based MOFs are not stable under basic conditions and some even can't retain their integrity in water. We expect that Ti-N-based MOFs could improve their stability, especially under basic conditions, though the synthesis of Ti-N based MOFs is a challenging task.

Ti-MOFs display excellent activities for photocatalysis. However, the photocatalytic efficiency is still low compared with some inorganic compounds. For a long-term target, an increase in the photocatalytic activity of one or two orders of magnitude in the case of photocatalytic hydrogen generation is needed. Though the capture chemistry of CO₂ in the presence of water has been discussed to highlight the importance of geometric constraints and the mediating role of water,^{260,261} more efforts are required to elucidate the mechanism of CO₂ reduction within Ti-MOFs. Moreover, the intrinsic photoactivity of Ti-MOFs needs to be further improved. Defect control and band gap engineering might be useful to enhance the photoactivity of Ti-MOFs. MOFs featuring periodic alignment chromophores and metal-oxo clusters open up the possibilities to set up a series of energy transfer systems, which can have insights into the energy transfer process. Though several energy transfer mechanisms have been proposed, theoretical calculations and modeling methods for a deeper understanding of the mechanism and charge migration kinetics were rarely reported.²⁶² Crystal engineering may allow us to control the spatial arrangement of Ti-MOFs, and the elaborate crystal structure analysis can provide a platform for in-depth investigations between structure–function relationships, allowing insights into further optimizing the fabrication of Ti-MOFs.

The morphology-dependent photocatalytic efficiency is scarcely investigated for Ti-MOFs. Discovering the mechanism of the surface heterojunction to explain the unique electron–hole separation phenomenon observed on the crystal facets of Ti-MOFs, along with precise control of the morphology and hierarchical assembly, can make significant progress in the elaboration of the photocatalytic mechanism of Ti-MOFs. The loading of photoactive molecules, metal particles, or inorganic and organic semiconductors with Ti-MOFs can be alternative methods to obviously improve their photocatalytic activity. It is still difficult to maintain the structural integrity of ligands

substituted with dye molecules when Ti-MOFs were modified to extend the light absorption spectrum. Taking into account the combination of high stability under extreme conditions and efficient photocatalytic activity, it's quite challenging to prepare Ti-MOF-based systems with well-defined structural integrity and high energy/mass transfer efficiency.

Overall, the research on Ti-MOFs is still in its infancy in which the photocatalytic applications are mainly restricted to MIL-125 and NH₂-MIL-125. It is urgent to deepen the utilization of other Ti-MOFs, especially based on infinite Ti-oxo chains and sheets. Note that the pore size and structure of MOFs play an important role in gas adsorption and separation; the applications of Ti-MOFs in gas adsorption and separation still need to be explored. Resolving some or all of the above-mentioned challenging tasks can efficiently push forward the development of Ti-MOFs for practical applications.

Conflicts of interest

There are no conflicts to declare.

Abbreviations

AB	4-Aminobenzoate
abz	4-Aminobenzoate
ATA	2-Aminoterephthalate
BA	<i>t</i> -Butylacetate
BDA	Benzene-1,4-dialdehyde
BDC	1,4-Bicarboxybenzene
BET	Brunauer–Emmett–Teller
BMA	Benzyl methacrylate
BPDA	4,4'-Biphenyldicarboxaldehyde
BPDC	4,4'-Biphenyldicarboxaldehyde
bpy	2,2'-Bipyridine
BTB	Benzene tribenzoate
BTC	1,3,5-Benzenetricarboxylate
cat	Catecholate
COF	Covalent organic framework
Cp ₂ Ti _{IV} Cl ₂	Dicyclopentadienyl titanium(IV) dichloride
dcdbdt	1,4-Dicarboxylbenzene-2,3-dithiolate
DEF	<i>N,N'</i> -Diethylformamide
DFT	Density functional theory
DMF	<i>N,N'</i> -Dimethylformamide
dmobpy	4,4'-Dimethoxy-2,2'-bipyridine
DMPO	5,5-Dimethyl-pyrroline- <i>N</i> -oxide
EA	Etidronic acid
EPR	Electron paramagnetic resonance
ESR	Electron spin resonance
HAc	Acetic acid
HOMO	Highest occupied molecular orbital
H ₂ cdc	<i>trans</i> -1,4-Cyclo-hexanedicarboxylic acid
H ₄ DOBDC	2,5-Dihydroxyterephthalic acid
H ₄ bdha	1,4-Dihydroxamic acid
H ₄ L	<i>N,N'</i> -Piperazinebismethylenephosphonic acid
H ₄ TBAPy	4,4',4'',4'''-Pyrene-1,3,6,8-tetrayl tetrabenzoic acid
H ₃ BTC	Trimesic acid
H ₆ THO	2,3,6,7,9,11-Hexahydroxytriphenylene

H ₄ mdip	3,3',5,5'-Tetracarboxydiphenylmethane
H ₃ TCA	4,4',4''-Nitrilotribenzoic acid
H ₃ BTCA	Tris(4'-carboxybiphenyl)amine
LMCT	Ligand-to-metal charge transfer
LUMO	Lowest unoccupied molecular orbital
MB	Methylene blue
MMA	Methyl methacrylate
MOFs	Metal-organic frameworks
NDC	2,6-Naphthalenedicarboxylate
NPs	Nanoparticles
NMR	Nuclear magnetic resonance
PL	Photoluminescence
PSE	Post-synthetic exchange
PSM	Post-synthetic modification
PXRD	Powder X-ray diffraction
RhB	Rhodamine B
SBU	Secondary building units
tatb	4,4',4''- <i>s</i> -Triazine-2,4,6-tribenzoic acid
TBP	5,10,15,20-Tetra(4-pyridyl)porphyrin
TCP	4,4',4'',4'''-(Porphyrin-5,10,15,20-tetrayl) tetrabenzoate
TDHT	2,4,6-Tri(3,4-dihydroxyphenyl)-1,3,5-triazine
TEMPO	2,2,6,6-Tetramethylpiperidinyloxy
TEOA	Triethanolamine
THF	Tetrahydrofuran
TOF	Turnover frequency
TON	Turnover number
Ti(i-OPr) ₄	Titanium tetraisopropoxide
TMP	2,2,6,6-Tetramethyl-4-piperidone
tpy	2,2',6',2'''-Terpyridine
UV	Ultraviolet
XRD	X-ray diffraction

Acknowledgements

This work was supported by the Zhejiang Provincial Natural Science Foundation of China (LY20E020001) and National Natural Science Foundation of China (51672251). J. G. acknowledges the Fundamental Research Funds of Zhejiang Sci-Tech University (2019Q007). Q. Z. Acknowledges AcRF Tier 1 (Grants RG 111/17, RG 2/17, RG 114/16, and RG 113/18) and Tier 2 (Grants MOE 2017-T2-1-021 and MOE 2018-T2-1-070), Singapore.

References

- 1 R. F. Service, *Science*, 2019, **365**, 108.
- 2 S. Cao, L. Piao and X. Chen, *Trends Chem.*, 2020, **2**, 57–70.
- 3 I. Ghosh, J. Khamrai, A. Savateev, N. Shlapakov, M. Antonietti and B. König, *Science*, 2019, **365**, 360–366.
- 4 D. J. Nürnberg, J. Morton, S. Santabarbara, A. Telfer, P. Joliot, L. A. Antonaru, A. V. Ruban, T. Cardona, E. Krausz and A. Boussac, *Science*, 2018, **360**, 1210–1213.
- 5 E. Kabir, P. Kumar, S. Kumar, A. A. Adelodun and K.-H. Kim, *Renewable Sustainable Energy Rev.*, 2018, **82**, 894–900.
- 6 N. S. Lewis, *Science*, 2016, **351**, aad1920.
- 7 D. M. Schultz and T. P. Yoon, *Science*, 2014, **343**, 1239176.

- 8 C. Xu, P. R. Anusuyadevi, C. Aymonier, R. Luque and S. Marre, *Chem. Soc. Rev.*, 2019, **48**, 3868–3902.
- 9 X. Yang and D. Wang, *ACS Appl. Energy Mater.*, 2018, **1**, 6657–6693.
- 10 B. Wang, W. Chen, Y. Song, G. Li, W. Wei, J. Fang and Y. Sun, *Catal. Today*, 2018, **311**, 23–39.
- 11 J. W. Ager and A. A. Lapkin, *Science*, 2018, **360**, 707–708.
- 12 J. Hao, X. Xu, H. Fei, L. Li and B. Yan, *Adv. Mater.*, 2018, **30**, 1705634.
- 13 Y. Fang, Y. Ma, M. Zheng, P. Yang, A. M. Asiri and X. Wang, *Coord. Chem. Rev.*, 2018, **373**, 83–115.
- 14 C. Gao, J. Wang, H. Xu and Y. Xiong, *Chem. Soc. Rev.*, 2017, **46**, 2799–2823.
- 15 M. Halmann, *Nature*, 1978, **275**, 115–116.
- 16 T. Inoue, A. Fujishima, S. Konishi and K. Honda, *Nature*, 1979, **277**, 637–638.
- 17 A. Meng, L. Zhang, B. Cheng and J. Yu, *Adv. Mater.*, 2019, **31**, 1807660.
- 18 Y. Ma, X. Wang, Y. Jia, X. Chen, H. Han and C. Li, *Chem. Rev.*, 2014, **114**, 9987–10043.
- 19 J. Balajka, M. A. Hines, W. J. DeBenedetti, M. Komora, J. Pavelec, M. Schmid and U. Diebold, *Science*, 2018, **361**, 786–789.
- 20 S. G. Ullattil, S. B. Narendranath, S. C. Pillai and P. Periyat, *Chem. Eng. J.*, 2018, **343**, 708–736.
- 21 S. Selcuk, X. Zhao and A. Selloni, *Nat. Mater.*, 2018, **17**, 923–928.
- 22 Z. Zhao, X. Zhang, G. Zhang, Z. Liu, D. Qu, X. Miao, P. Feng and Z. Sun, *Nano Res.*, 2015, **8**, 4061–4071.
- 23 Q. Wang and D. Astruc, *Chem. Rev.*, 2020, **120**, 1438–1511.
- 24 C. H. Hendon, A. J. Rieth, M. D. Korzyński and M. Dinç, *ACS Cent. Sci.*, 2017, **3**, 554–563.
- 25 H. Furukawa, K. E. Cordova, M. O’Keeffe and O. M. Yaghi, *Science*, 2013, **341**, 1230444.
- 26 P. G. Boyd, A. Chidambaram, E. Garcia-Diez, C. P. Ireland, T. D. Daff, R. Bounds, A. Gladysiak, P. Schouwink, S. M. Moosavi, M. M. Maroto-Valer, J. A. Reimer, J. A. R. Navarro, T. K. Woo, S. Garcia, K. C. Stylianou and B. Smit, *Nature*, 2019, **576**, 253–256.
- 27 A. Pulido, L. Chen, T. Kaczorowski, D. Holden, M. A. Little, S. Y. Chong, B. J. Slater, D. P. McMahon, B. Bonillo, C. J. Stackhouse, A. Stephenson, C. M. Kane, R. Clowes, T. Hasell, A. I. Cooper and G. M. Day, *Nature*, 2017, **543**, 657–664.
- 28 B. Li, H.-M. Wen, Y. Cui, W. Zhou, G. Qian and B. Chen, *Adv. Mater.*, 2016, **28**, 8819–8860.
- 29 Y. Cui, B. Li, H. He, W. Zhou, B. Chen and G. Qian, *Acc. Chem. Res.*, 2016, **49**, 483–493.
- 30 R.-B. Lin, S. Xiang, H. Xing, W. Zhou and B. Chen, *Coord. Chem. Rev.*, 2019, **378**, 87–103.
- 31 H. Li, L. Li, R.-B. Lin, W. Zhou, S. Xiang, B. Chen and Z. Zhang, *EnergyChem*, 2019, **1**, 100006.
- 32 K.-J. Chen, D. G. Madden, S. Mukherjee, T. Pham, K. A. Forrest, A. Kumar, B. Space, J. Kong, Q.-Y. Zhang and M. J. Zaworotko, *Science*, 2019, **366**, 241–246.
- 33 H. Yang, Y. Wang, R. Krishna, X. Jia, Y. Wang, A. N. Hong, C. Dang, H. E. Castillo, X. Bu and P. Feng, *J. Am. Chem. Soc.*, 2020, **142**, 2222–2227.
- 34 J. Gao, X. Qian, R. Lin, R. Krishna, H. Wu, W. Zhou and B. Chen, *Angew. Chem., Int. Ed.*, 2020, **59**, 4396–4400.
- 35 L. Li, R.-B. Lin, R. Krishna, H. Li, S. Xiang, H. Wu, J. Li, W. Zhou and B. Chen, *Science*, 2018, **362**, 443–446.
- 36 X. Zhao, Y. Wang, D.-S. Li, X. Bu and P. Feng, *Adv. Mater.*, 2018, **30**, 1705189.
- 37 A. Bavykina, N. Kolobov, I. S. Khan, J. A. Bau, A. Ramirez and J. Gascon, *Chem. Rev.*, 2020, DOI: 10.1021/acs.chemrev.1029b00685.
- 38 A. Dhakshinamoorthy, A. M. Asiri and H. Garcia, *Adv. Mater.*, 2019, **31**, 1900617.
- 39 C. S. Diercks, Y. Liu, K. E. Cordova and O. M. Yaghi, *Nat. Mater.*, 2018, **17**, 301–307.
- 40 L. Zhu, X.-Q. Liu, H.-L. Jiang and L.-B. Sun, *Chem. Rev.*, 2017, **117**, 8129–8176.
- 41 Y.-B. Huang, J. Liang, X.-S. Wang and R. Cao, *Chem. Soc. Rev.*, 2017, **46**, 126–157.
- 42 W. Zhou, D.-D. Huang, Y.-P. Wu, J. Zhao, T. Wu, J. Zhang, D.-S. Li, C. Sun, P. Feng and X. Bu, *Angew. Chem., Int. Ed.*, 2019, **58**, 4227–4231.
- 43 L. Jiao, Y. Wang, H. L. Jiang and Q. Xu, *Adv. Mater.*, 2018, **30**, 1703663.
- 44 Y. Li, T. Zhao, M. Lu, Y. Wu, Y. Xie, H. Xu, J. Gao, J. Yao, G. Qian and Q. Zhang, *Small*, 2019, **15**, 1901940.
- 45 Y. Li, M. Lu, Y. Wu, H. Xu, J. Gao and J. Yao, *Adv. Mater. Interfaces*, 2019, **6**, 1900290.
- 46 J. Gao, J. Cong, Y. Wu, L. Sun, J. Yao and B. Chen, *ACS Appl. Energy Mater.*, 2018, **1**, 5140–5144.
- 47 Y. Zhang, S. Yuan, G. Day, X. Wang, X. Yang and H.-C. Zhou, *Coord. Chem. Rev.*, 2018, **354**, 28–45.
- 48 L. E. Kreno, K. Leong, O. K. Farha, M. Allendorf, R. P. Van Deyne and J. T. Hupp, *Chem. Rev.*, 2012, **112**, 1105–1125.
- 49 Y. Cui, Y. Yue, G. Qian and B. Chen, *Chem. Rev.*, 2012, **112**, 1126–1162.
- 50 Z. Dou, J. Yu, Y. Cui, Y. Yang, Z. Wang, D. Yang and G. Qian, *J. Am. Chem. Soc.*, 2014, **136**, 5527–5530.
- 51 Y. Cui, B. Chen and G. Qian, *Coord. Chem. Rev.*, 2014, **273**, 76–86.
- 52 L. Wang, H. Xu, J. Gao, J. Yao and Q. Zhang, *Coord. Chem. Rev.*, 2019, **398**, 213016.
- 53 Y. Cui, J. Zhang, H. He and G. Qian, *Chem. Soc. Rev.*, 2018, **47**, 5740–5785.
- 54 Y. Xu, Q. Li, H. Xue and H. Pang, *Coord. Chem. Rev.*, 2018, **376**, 292–318.
- 55 S. Dang, Q.-L. Zhu and Q. Xu, *Nat. Rev. Mater.*, 2018, **3**, 17075.
- 56 H. Kim, S. Yang, S. R. Rao, S. Narayanan, E. A. Kapustin, H. Furukawa, A. S. Umans, O. M. Yaghi and E. N. Wang, *Science*, 2017, **356**, 430–434.
- 57 X. Cao, C. Tan, M. Sindoro and H. Zhang, *Chem. Soc. Rev.*, 2017, **46**, 2660–2677.
- 58 C. Jones, A. Tansell and T. Easun, *J. Mater. Chem. A*, 2016, **4**, 6714–6723.

- 59 H. He, E. Ma, Y. Cui, J. Yu, Y. Yang, T. Song, C.-D. Wu, X. Chen, B. Chen and G. Qian, *Nat. Commun.*, 2016, **7**, 1–7.
- 60 C. Li, K. Wang, J. Li and Q. Zhang, *Nanoscale*, 2020, **12**, 7870–7874.
- 61 K.-B. Wang, Q. Xun and Q. Zhang, *EnergyChem*, 2020, **2**, 100025.
- 62 Z. Wu, J. Xie, Z. J. Xu, S. Zhang and Q. Zhang, *J. Mater. Chem. A*, 2019, **7**, 4259–4290.
- 63 C. Doonan, R. Riccò, K. Liang, D. Bradshaw and P. Falcaro, *Acc. Chem. Res.*, 2017, **50**, 1423–1432.
- 64 P. Horcajada, R. Gref, T. Baati, P. K. Allan, G. Maurin, P. Couvreur, G. Ferey, R. E. Morris and C. Serre, *Chem. Rev.*, 2012, **112**, 1232–1268.
- 65 K. Lu, T. Aung, N. Guo, R. Weichselbaum and W. Lin, *Adv. Mater.*, 2018, **30**, 1707634.
- 66 X. Lian, Y. Fang, E. Joseph, Q. Wang, J. Li, S. Banerjee, C. Lollar, X. Wang and H.-C. Zhou, *Chem. Soc. Rev.*, 2017, **46**, 3386–3401.
- 67 L. Nie and Q. Zhang, *Inorg. Chem. Front.*, 2017, **4**, 1953–1962.
- 68 J. Gao, J. Miao, Y. Li, R. Ganguly, Y. Zhao, O. Lev, B. Liu and Q. Zhang, *Dalton Trans.*, 2015, **44**, 14354–14358.
- 69 D. Liu, X. Fan, X. Wang, D. Hu, C. Xue, Y. Liu, Y. Wang, X. Zhu, J. Guo, H. Lin, Y. Li, J. Zhong, D. Li, X. Bu, P. Feng and T. Wu, *Chem. Mater.*, 2019, **31**, 553–559.
- 70 H. Yang, J. Zhang, M. Luo, W. Wang, H. Lin, Y. Li, D. Li, P. Feng and T. Wu, *J. Am. Chem. Soc.*, 2018, **140**, 11189–11192.
- 71 X. Xu, W. Wang, D. Liu, D. Hu, T. Wu, X. Bu and P. Feng, *J. Am. Chem. Soc.*, 2018, **140**, 888–891.
- 72 J. Kou, C. Lu, J. Wang, Y. Chen, Z. Xu and R. S. Varma, *Chem. Rev.*, 2017, **117**, 1445–1514.
- 73 K. Shen, L. Zhang, X. Chen, L. Liu, D. Zhang, Y. Han, J. Chen, J. Long, R. Luque and Y. Li, *Science*, 2018, **359**, 206–210.
- 74 Y. Cui, B. Li, H. He, W. Zhou, B. Chen and G. Qian, *Acc. Chem. Res.*, 2016, **49**, 483–493.
- 75 K. G. M. Laurier, F. Vermoortele, R. Ameloot, D. E. De Vos, J. Hofkens and M. B. J. Roefiaers, *J. Am. Chem. Soc.*, 2013, **135**, 14488–14491.
- 76 L. Shi, L. Yang, H. Zhang, K. Chang, G. Zhao, T. Kako and J. Ye, *Appl. Catal., B*, 2018, **224**, 60–68.
- 77 X.-P. Wu, L. Gagliardi and D. G. Truhlar, *J. Am. Chem. Soc.*, 2018, **140**, 7904–7912.
- 78 L. Shi, T. Wang, H. Zhang, K. Chang, X. Meng, H. Liu and J. Ye, *Adv. Sci.*, 2015, **2**, 1500006.
- 79 X. Z. Fang, Q. C. Shang, Y. Wang, L. Jiao, T. Yao, Y. F. Li, Q. Zhang, Y. Luo and H. L. Jiang, *Adv. Mater.*, 2018, **30**, 1705112.
- 80 Q. H. Yang, Q. Xu and H. L. Jiang, *Chem. Soc. Rev.*, 2017, **46**, 4774–4808.
- 81 J.-D. Xiao and H.-L. Jiang, *Acc. Chem. Res.*, 2019, **52**, 356–366.
- 82 Y. Liu, Z. Liu, D. Huang, M. Cheng, G. Zeng, C. Lai, C. Zhang, C. Zhou, W. Wang, D. Jiang, H. Wang and B. Shao, *Coord. Chem. Rev.*, 2019, **388**, 63–78.
- 83 D. Li, H.-Q. Xu, L. Jiao and H.-L. Jiang, *EnergyChem*, 2019, **1**, 100005.
- 84 E. A. Dolgoplova, A. M. Rice, C. R. Martin and N. B. Shustova, *Chem. Soc. Rev.*, 2018, **47**, 4710–4728.
- 85 Q. Wang, Y. Zhang, H. Lin and J. Zhu, *Chem.–Eur. J.*, 2019, **25**, 14026–14035.
- 86 X. Deng, R. Li, S. Wu, L. Wang, J. Hu, J. Ma, W. Jiang, N. Zhang, X. Zheng and C. Gao, *J. Am. Chem. Soc.*, 2019, **141**, 10924–10929.
- 87 Y. Shi, A.-F. Yang, C.-S. Cao and B. Zhao, *Coord. Chem. Rev.*, 2019, **390**, 50–75.
- 88 S. Kampouri and K. C. Stylianou, *ACS Catal.*, 2019, **9**, 4247–4270.
- 89 G. Lan, Y.-Y. Zhu, S. S. Veroneau, Z. Xu, D. Micheroni and W. Lin, *J. Am. Chem. Soc.*, 2018, **140**, 5326–5329.
- 90 X.-K. Wang, J. Liu, L. Zhang, L.-Z. Dong, S.-L. Li, Y.-H. Kan, D.-S. Li and Y.-Q. Lan, *ACS Catal.*, 2019, **9**, 1726–1732.
- 91 Z.-H. Yan, M.-H. Du, J. Liu, S. Jin, C. Wang, G.-L. Zhuang, X.-J. Kong, L.-S. Long and L.-S. Zheng, *Nat. Commun.*, 2018, **9**, 3353.
- 92 Y. Xiao, Y. Qi, X. Wang, X. Wang, F. Zhang and C. Li, *Adv. Mater.*, 2018, **30**, 1803401.
- 93 X. Feng, Y. Pi, Y. Song, C. Brzezinski, Z. Xu, Z. Li and W. Lin, *J. Am. Chem. Soc.*, 2020, **142**, 690–695.
- 94 A. Dhakshinamoorthy, Z. Li and H. Garcia, *Chem. Soc. Rev.*, 2018, **47**, 8134–8172.
- 95 D. Sun and Z. Li, *Chin. J. Chem.*, 2017, **35**, 135–147.
- 96 X. Deng, Z. Li and H. Garcia, *Chem.–Eur. J.*, 2017, **23**, 11189–11209.
- 97 Y. Chen, D. Wang, X. Deng and Z. Li, *Catal. Sci. Technol.*, 2017, **7**, 4893–4904.
- 98 P. Z. Moghadam, A. Li, S. B. Wiggin, A. Tao, A. G. Maloney, P. A. Wood, S. C. Ward and D. Fairen-Jimenez, *Chem. Mater.*, 2017, **29**, 2618–2625.
- 99 S. Wang, T. Kitao, N. Guillou, M. Wahiduzzaman, C. Martineau-Corcós, F. Nouar, A. Tissot, L. Binet, N. Ramsahye, S. Devautour-Vinot, S. Kitagawa, S. Seki, Y. Tsutsui, V. Briois, N. Steunou, G. Maurin, T. Uemura and C. Serre, *Nat. Commun.*, 2018, **9**, 1660.
- 100 C. Li, H. Xu, J. Gao, W. Du, L. Shangguan, X. Zhang, R.-B. Lin, H. Wu, W. Zhou and X. Liu, *J. Mater. Chem. A*, 2019, **7**, 11928–11933.
- 101 Q.-G. Zhai, X. Bu, C. Mao, X. Zhao, L. Daemen, Y. Cheng, A. J. Ramirez-Cuesta and P. Feng, *Nat. Commun.*, 2016, **7**, 1–9.
- 102 F.-Y. Yi, H. Yang, X. Zhao, P. Feng and X. Bu, *Angew. Chem., Int. Ed.*, 2019, **58**, 2889–2892.
- 103 H. Yang, F. Peng, C. Dang, Y. Wang, D. Hu, X. Zhao, P. Feng and X. Bu, *J. Am. Chem. Soc.*, 2019, **141**, 9808–9812.
- 104 X. Zhao, H. Yang, E. T. Nguyen, J. Padilla, X. Chen, P. Feng and X. Bu, *J. Am. Chem. Soc.*, 2018, **140**, 13566–13569.
- 105 X. Zhang, Y. Li, C. Van Goethem, K. Wan, W. Zhang, J. Luo, I. F. J. Vankelecom and J. Fransaer, *Matter*, 2019, **1**, 1285–1292.
- 106 Q. Zhang, Z. Wu, Y. Lv, Y. Li, Y. Zhao, R. Zhang, Y. Xiao, X. Shi, D. Zhang, R. Hua, J. Yao, J. Guo, R. Huang, Y. Cui, Z. Kang, S. Goswami, L. Robison, K. Song, X. Li, Y. Han,

- L. Chi, O. K. Farha and G. Lu, *Angew. Chem., Int. Ed.*, 2019, **58**, 1123–1128.
- 107 R. Wei, H.-Y. Chi, X. Li, D. Lu, Y. Wan, C.-W. Yang and Z. Lai, *Adv. Funct. Mater.*, 2020, **30**, 1907089.
- 108 H. Al-Kutubi, J. Gascon, E. J. Sudhölter and L. Rassaei, *ChemElectroChem*, 2015, **2**, 462–474.
- 109 M. Rubio-Martinez, C. Avci-Camur, A. W. Thornton, I. Imaz, D. MasPOCH and M. R. Hill, *Chem. Soc. Rev.*, 2017, **46**, 3453–3480.
- 110 I. Thomas-Hillman, A. Laybourn, C. Dodds and S. W. Kingman, *J. Mater. Chem. A*, 2018, **6**, 11564–11581.
- 111 A. Laybourn, J. Katrib, R. S. Ferrari-John, C. G. Morris, S. Yang, O. Udoudo, T. L. Easun, C. Dodds, N. R. Champness and S. W. Kingman, *J. Mater. Chem. A*, 2017, **5**, 7333–7338.
- 112 J. Ren, X. Dyosiba, N. M. Musyoka, H. W. Langmi, M. Mathe and S. Liao, *Coord. Chem. Rev.*, 2017, **352**, 187–219.
- 113 Z. Lin, D. S. Wragg and R. E. Morris, *Chem. Commun.*, 2006, 2021–2023.
- 114 I. Brekalo, W. Yuan, C. Mottillo, Y. Lu, Y. Zhang, J. Casaban, K. T. Holman, S. L. James, F. Duarte, P. A. Williams, K. D. M. Harris and T. Friscic, *Chem. Sci.*, 2020, **11**, 2141–2147.
- 115 I. Brekalo, C. M. Kane, A. N. Ley, J. R. Ramirez, T. Friscic and K. T. Holman, *J. Am. Chem. Soc.*, 2018, **140**, 10104–10108.
- 116 H. Sakamoto, R. Matsuda and S. Kitagawa, *Dalton Trans.*, 2012, **41**, 3956–3961.
- 117 J. Zhao, X. Liu, Y. Wu, D.-S. Li and Q. Zhang, *Coord. Chem. Rev.*, 2019, **391**, 30–43.
- 118 P. Li, F.-F. Cheng, W.-W. Xiong and Q. Zhang, *Inorg. Chem. Front.*, 2018, **5**, 2693–2708.
- 119 Y. P. Wu, W. Zhou, J. Zhao, W. W. Dong, Y. Q. Lan, D. S. Li, C. Sun and X. Bu, *Angew. Chem., Int. Ed.*, 2017, **56**, 13001–13005.
- 120 W. W. Xiong and Q. Zhang, *Angew. Chem., Int. Ed.*, 2015, **54**, 11616–11623.
- 121 H.-S. Lu, L. Bai, W.-W. Xiong, P. Li, J. Ding, G. Zhang, T. Wu, Y. Zhao, J.-M. Lee and Y. Yang, *Inorg. Chem.*, 2014, **53**, 8529–8537.
- 122 J. Gao, K. Ye, L. Yang, W.-W. Xiong, L. Ye, Y. Wang and Q. Zhang, *Inorg. Chem.*, 2014, **53**, 691–693.
- 123 J. Gao, K. Ye, M. He, W.-W. Xiong, W. Cao, Z. Y. Lee, Y. Wang, T. Wu, F. Huo and X. Liu, *J. Solid State Chem.*, 2013, **206**, 27–31.
- 124 C. Serre, J. A. Groves, P. Lightfoot, A. M. Z. Slawin, P. A. Wright, N. Stock, T. Bein, M. Haouas, F. Taulelle and G. Férey, *Chem. Mater.*, 2006, **18**, 1451–1457.
- 125 B. Chakraborty and I. A. Weinstock, *Coord. Chem. Rev.*, 2019, **382**, 85–102.
- 126 W.-H. Fang, L. Zhang and J. Zhang, *Chem. Soc. Rev.*, 2018, **47**, 404–421.
- 127 L. Mino, M. Signorile, V. Crocellà and C. Lamberti, *Chem. Rec.*, 2019, **19**, 1319–1336.
- 128 Y.-J. Liu, W.-H. Fang, L. Zhang and J. Zhang, *Coord. Chem. Rev.*, 2020, **404**, 213099.
- 129 N. Li, J. Liu, J.-J. Liu, L.-Z. Dong, S.-L. Li, B.-X. Dong, Y.-H. Kan and Y.-Q. Lan, *Angew. Chem., Int. Ed.*, 2019, **58**, 17260–17264.
- 130 X. Fan, J. Wang, K. Wu, L. Zhang and J. Zhang, *Angew. Chem., Int. Ed.*, 2019, **58**, 1320–1323.
- 131 S. Chen, Z.-N. Chen, W.-H. Fang, W. Zhuang, L. Zhang and J. Zhang, *Angew. Chem., Int. Ed.*, 2019, **58**, 10932–10935.
- 132 C. Zhao, Y.-Z. Han, S. Dai, X. Chen, J. Yan, W. Zhang, H. Su, S. Lin, Z. Tang, B. K. Teo and N. Zheng, *Angew. Chem., Int. Ed.*, 2017, **56**, 16252–16256.
- 133 Z. Jiang, J. Liu, M. Gao, X. Fan, L. Zhang and J. Zhang, *Adv. Mater.*, 2017, **29**, 1603369.
- 134 Y.-P. He, L.-B. Yuan, G.-H. Chen, Q.-P. Lin, F. Wang, L. Zhang and J. Zhang, *J. Am. Chem. Soc.*, 2017, **139**, 16845–16851.
- 135 L. Rozes and C. Sanchez, *Chem. Soc. Rev.*, 2011, **40**, 1006–1030.
- 136 A. Cadiou, L. S. Xie, N. Kolobov, A. Shkurenko, M. Qureshi, M. R. Tchalala, S. S. Park, A. Bavykina, M. Eddaoudi, M. Dinca, C. H. Hendon and J. Gascon, *Chem. Mater.*, 2020, **32**, 97–104.
- 137 C. A. Trickett, T. M. O. Popp, J. Su, C. Yan, J. Weisberg, A. Huq, P. Urban, J. Jiang, M. J. Kalmutzki, Q. Liu, J. Baek, M. P. Head-Gordon, G. A. Somorjai, J. A. Reimer and O. M. Yaghi, *Nat. Chem.*, 2019, **11**, 170–176.
- 138 I. A. Lazaro and R. S. Forgan, *Coord. Chem. Rev.*, 2019, **380**, 230–259.
- 139 Z. Chen, S. L. Hanna, L. R. Redfern, D. Alezi, T. Islamoglu and O. K. Farha, *Coord. Chem. Rev.*, 2019, **386**, 32–49.
- 140 S. Wang, J. S. Lee, M. Wahiduzzaman, J. Park, M. Muschi, C. Martineau-Corcós, A. Tissot, K. H. Cho, J. Marrot, W. Shepard, G. Maurin, J.-S. Chang and C. Serre, *Nat. Energy*, 2018, **3**, 985–993.
- 141 Y. Bai, Y. Dou, L.-H. Xie, W. Rutledge, J.-R. Li and H.-C. Zhou, *Chem. Soc. Rev.*, 2016, **45**, 2327–2367.
- 142 Y. Keum, S. Park, Y. P. Chen and J. Park, *Angew. Chem., Int. Ed.*, 2018, **57**, 14852–14856.
- 143 S. Yuan, T.-F. Liu, D. Feng, J. Tian, K. Wang, J. Qin, Q. Zhang, Y.-P. Chen, M. Bosch and L. Zou, *Chem. Sci.*, 2015, **6**, 3926–3930.
- 144 J. Gao, J. Miao, P.-Z. Li, W. Y. Teng, L. Yang, Y. Zhao, B. Liu and Q. Zhang, *Chem. Commun.*, 2014, **50**, 3786–3788.
- 145 H. Assi, L. C. Pardo Pérez, G. Mouchaham, F. Ragon, M. Nasalevich, N. Guillou, C. Martineau, H. Chevreau, F. Kapteijn and J. Gascon, *Inorg. Chem.*, 2016, **55**, 7192–7199.
- 146 N. T. Nguyen, H. Furukawa, F. Gándara, C. A. Trickett, H. M. Jeong, K. E. Cordova and O. M. Yaghi, *J. Am. Chem. Soc.*, 2015, **137**, 15394–15397.
- 147 N. M. Padial, J. Castells-Gil, N. Almora-Barrios, M. a. Romero-Angel, I. Da Silva, M. Barawi, A. García-Sánchez, V. c. A. de la Peña O'Shea and C. Marti-Gastaldo, *J. Am. Chem. Soc.*, 2019, **141**, 13124–13133.
- 148 J. Cao, W. Ma, K. Lyu, L. Zhuang, H. Cong and H. Deng, *Chem. Sci.*, 2020, **11**, 3978–3985.

- 149 Y. P. Zhu, J. Yin, E. Abou-Hamad, X. Liu, W. Chen, T. Yao, O. F. Mohammed and H. N. Alshareef, *Adv. Mater.*, 2020, **31**, 1906368.
- 150 J. A. Mason, L. E. Darago, W. W. Lukens Jr and J. R. Long, *Inorg. Chem.*, 2015, **54**, 10096–10104.
- 151 Y. Song, Z. Li, Y. Zhu, X. Feng, J. S. Chen, M. Kaufmann, C. Wang and W. Lin, *J. Am. Chem. Soc.*, 2019, **141**, 12219–12223.
- 152 B. Bueken, F. Vermoortele, D. E. Vanpoucke, H. Reinsch, C. C. Tsou, P. Valvekens, T. De Baerdemaeker, R. Ameloot, C. E. Kirschhock and V. Van Speybroeck, *Angew. Chem., Int. Ed.*, 2015, **54**, 13912–13917.
- 153 H. L. Nguyen, F. Gándara, H. Furukawa, T. L. Doan, K. E. Cordova and O. M. Yaghi, *J. Am. Chem. Soc.*, 2016, **138**, 4330–4333.
- 154 H. L. Nguyen, T. T. Vu, D. Le, T. L. Doan, V. Q. Nguyen and N. T. Phan, *ACS Catal.*, 2017, **7**, 338–342.
- 155 M. Dan-Hardi, C. Serre, T. Frot, L. Rozes, G. Maurin, C. Sanchez and G. Férey, *J. Am. Chem. Soc.*, 2009, **131**, 10857–10859.
- 156 Y. Fu, D. Sun, Y. Chen, R. Huang, Z. Ding, X. Fu and Z. Li, *Angew. Chem., Int. Ed.*, 2012, **51**, 3364–3367.
- 157 S. Wang, H. Reinsch, N. Heymans, M. Wahiduzzaman, C. Martineau-Corcós, G. De Weireld, G. Maurin and C. Serre, *Matter*, 2020, **2**, 440–450.
- 158 G. Lan, K. Ni, S. S. Veroneau, X. Feng, G. T. Nash, T. Luo, Z. Xu and W. Lin, *J. Am. Chem. Soc.*, 2019, **141**, 4204–4208.
- 159 A. Cadiou, N. Kolobov, S. Srinivasan, M. Goesten, H. Haspel, A. Bavykina, M. Tchalala, P. Maity, A. Goryachev, A. Poryvaev, M. Eddaoudi, M. Fedin, O. Mohammed and J. Gascon, *Angew. Chem., Int. Ed.*, 2020, DOI: 10.1002/anie.202000158.
- 160 S. Smolders, T. Willhammar, A. Krajnc, K. Sentosun, M. T. Wharmby, K. A. Lomachenko, S. Bals, G. Mali, M. B. Roefiaers and D. E. De Vos, *Angew. Chem., Int. Ed.*, 2019, **58**, 9160–9165.
- 161 S. Yuan, J.-S. Qin, H.-Q. Xu, J. Su, D. Rossi, Y. Chen, L. Zhang, C. Lollar, Q. Wang and H.-L. Jiang, *ACS Cent. Sci.*, 2018, **4**, 105–111.
- 162 J. Castells-Gil, N. M. Padial, N. Almora-Barrios, J. Albero, A. R. Ruiz-Salvador, J. González-Platas, H. García and C. Martí-Gastaldo, *Angew. Chem., Int. Ed.*, 2018, **57**, 8453–8457.
- 163 H. Chun and D. Moon, *Cryst. Growth Des.*, 2017, **17**, 2140–2146.
- 164 J. Castells-Gil, N. M. Padial, N. Almora-Barrios, I. Da Silva, D. Mateo, J. Albero, H. García and C. Martí-Gastaldo, *Chem. Sci.*, 2019, **10**, 4313–4321.
- 165 A. M. Antonio, J. Rosenthal and E. D. Bloch, *J. Am. Chem. Soc.*, 2019, **141**, 11383–11387.
- 166 X. Feng, Y. Song, J. S. Chen, Z. Li, E. Y. Chen, M. Kaufmann, C. Wang and W. Lin, *Chem. Sci.*, 2019, **10**, 2193–2198.
- 167 C. Wang, C. Liu, X. He and Z. M. Sun, *Chem. Commun.*, 2017, **53**, 11670–11673.
- 168 J.-L. Hou, W. Luo, Y. Guo, P. Zhang, S. Yang, Q.-Y. Zhu and J. Dai, *Inorg. Chem.*, 2017, **56**, 6451–6458.
- 169 Y. Zhong, B. Cheng, C. Park, A. Ray, S. Brown, F. Mujid, J.-U. Lee, H. Zhou, J. Suh, K.-H. Lee, A. J. Mannix, K. Kang, S. J. Sibener, D. A. Muller and J. Park, *Science*, 2019, **366**, 1379–1384.
- 170 Z. W. Jiang, Y. C. Zou, T. T. Zhao, S. J. Zhen, Y. F. Li and C. Z. Huang, *Angew. Chem., Int. Ed.*, 2020, **59**, 3300–3306.
- 171 Q. Huang, J. Liu, L. Feng, Q. Wang, W. Guan, L.-Z. Dong, L. ZHANG, L.-K. Yan, Y.-Q. Lan and H.-C. Zhou, *Natl. Sci. Rev.*, 2020, **7**, 53–63.
- 172 E. X. Chen, M. Qiu, Y. F. Zhang, Y. S. Zhu, L. Y. Liu, Y. Y. Sun, X. H. Bu, J. Zhang and Q. P. Lin, *Adv. Mater.*, 2018, **30**, 1704388.
- 173 W. Zhang, W. Lai and R. Cao, *Chem. Rev.*, 2017, **117**, 3717–3797.
- 174 H.-Q. Xu, J. Hu, D. Wang, Z. Li, Q. Zhang, Y. Luo, S.-H. Yu and H.-L. Jiang, *J. Am. Chem. Soc.*, 2015, **137**, 13440–13443.
- 175 W.-Y. Gao, M. Chrzanowski and S. Ma, *Chem. Soc. Rev.*, 2014, **43**, 5841–5866.
- 176 T. Frot, S. Cochet, G. Laurent, C. Sassoey, M. Popall, C. Sanchez and L. Rozes, *Eur. J. Inorg. Chem.*, 2010, 5650–5659.
- 177 Z. Xu, H. Fu, T. Wen, L. Zhang and J. Zhang, *Int. J. Hydrogen Energy*, 2017, **42**, 24737–24743.
- 178 S.-N. Kim, J. Kim, H.-Y. Kim, H.-Y. Cho and W.-S. Ahn, *Catal. Today*, 2013, **204**, 85–93.
- 179 A. Dhakshinamoorthy, A. M. Asiri and H. García, *Angew. Chem., Int. Ed.*, 2016, **55**, 5414–5445.
- 180 T. Tachikawa, S. Tojo, M. Fujitsuka, T. Sekino and T. Majima, *J. Phys. Chem. B*, 2006, **110**, 14055–14059.
- 181 M. A. Nasalevich, C. H. Hendon, J. G. Santaclara, K. Svane, B. Van Der Linden, S. L. Veber, M. V. Fedin, A. J. Houtepen, M. A. Van Der Veen and F. Kapteijn, *Sci. Rep.*, 2016, **6**, 23676.
- 182 D. L. Dexter, *J. Chem. Phys.*, 1953, **21**, 836–850.
- 183 J. Low, J. Yu, M. Jaroniec, S. Wageh and A. A. Al-Ghamdi, *Adv. Mater.*, 2017, **29**, 1601694.
- 184 C. H. Hendon, D. Tiana, M. Fontecave, C. m. Sanchez, L. D'arras, C. Sassoey, L. Rozes, C. Mellot-Draznieks and A. Walsh, *J. Am. Chem. Soc.*, 2013, **135**, 10942–10945.
- 185 M. A. Nasalevich, M. G. Goesten, T. J. Savenije, F. Kapteijn and J. Gascon, *Chem. Commun.*, 2013, **49**, 10575–10577.
- 186 M. W. Logan, S. Ayad, J. D. Adamson, T. Dilbeck, K. Hanson and F. J. Uribe-Romo, *J. Mater. Chem. A*, 2017, **5**, 11854–11863.
- 187 D. Sun, W. Liu, M. Qiu, Y. Zhang and Z. Li, *Chem. Commun.*, 2015, **51**, 2056–2059.
- 188 Y. Lee, S. Kim, J. K. Kang and S. M. Cohen, *Chem. Commun.*, 2015, **51**, 5735–5738.
- 189 J. G. Santaclara, A. I. Olivos-Suarez, A. Gonzalez-Nelson, D. Osadchii, M. A. Nasalevich, M. A. Van Der Veen, F. Kapteijn, A. M. Sheveleva, S. L. Veber and M. V. Fedin, *Chem. Mater.*, 2017, **29**, 8963–8967.
- 190 A. Gómez-Avilés, M. Peñas-Garzón, J. Bedia, D. Dionysiou, J. Rodríguez and C. Belver, *Appl. Catal., B*, 2019, **253**, 253–262.

- 191 K. M. Choi, D. Kim, B. Rungtaweevoranit, C. A. Trickett, J. T. D. Barmanbek, A. S. Alshammari, P. Yang and O. M. Yaghi, *J. Am. Chem. Soc.*, 2017, **139**, 356–362.
- 192 C. Y. Lee, O. K. Farha, B. J. Hong, A. A. Sarjeant, S. T. Nguyen and J. T. Hupp, *J. Am. Chem. Soc.*, 2011, **133**, 15858–15861.
- 193 Y. Song, Y. Pi, X. Feng, K. Ni, Z. Xu, J. S. Chen, Z. Li and W. Lin, *J. Am. Chem. Soc.*, 2020, **142**(15), 6866–6871.
- 194 X. Feng, Y. Pi, Y. Song, C. Brzezinski, Z. Xu, Z. Li and W. Lin, *J. Am. Chem. Soc.*, 2020, **142**, 690–695.
- 195 Y.-Y. Zhu, G. Lan, Y. Fan, S. S. Veroneau, Y. Song, D. Micheroni and W. Lin, *Angew. Chem., Int. Ed.*, 2018, **57**, 14090–14094.
- 196 S. Pullen, H. Fei, A. Orthaber, S. M. Cohen and S. Ott, *J. Am. Chem. Soc.*, 2013, **135**, 16997–17003.
- 197 T. Toyao, M. Saito, S. Dohshi, K. Mochizuki, M. Iwata, H. Higashimura, Y. Horiuchi and M. Matsuoka, *Chem. Commun.*, 2014, **50**, 6779–6781.
- 198 H. R. Moon, D.-W. Lim and M. P. Suh, *Chem. Soc. Rev.*, 2013, **42**, 1807–1824.
- 199 C. R. Kim, T. Uemura and S. Kitagawa, *Chem. Soc. Rev.*, 2016, **45**, 3828–3845.
- 200 J. He, Z. Yan, J. Wang, J. Xie, L. Jiang, Y. Shi, F. Yuan, F. Yu and Y. Sun, *Chem. Commun.*, 2013, **49**, 6761–6763.
- 201 B. Xia, J. Ran, S. Chen, L. Song, X. Zhang, L. Jing and S.-Z. Qiao, *Nanoscale*, 2019, **11**, 8304–8309.
- 202 G. Liu, C. Zhen, Y. Kang, L. Wang and H.-M. Cheng, *Chem. Soc. Rev.*, 2018, **47**, 6410–6444.
- 203 Y.-C. Zhang, N. Afzal, L. Pan, X. Zhang and J.-J. Zou, *Adv. Sci.*, 2019, **6**, 1900053.
- 204 L. Lin, Z. Yu and X. Wang, *Angew. Chem., Int. Ed.*, 2019, **58**, 6164–6175.
- 205 B.-H. Lee, S. Park, M. Kim, A. K. Sinha, S. C. Lee, E. Jung, W. J. Chang, K.-S. Lee, J. H. Kim, S.-P. Cho, H. Kim, K. T. Nam and T. Hyeon, *Nat. Mater.*, 2019, **18**, 620–626.
- 206 Y. Horiuchi, T. Toyao, M. Saito, K. Mochizuki, M. Iwata, H. Higashimura, M. Anpo and M. Matsuoka, *J. Phys. Chem. C*, 2012, **116**, 20848–20853.
- 207 L. Shen, M. Luo, L. Huang, P. Feng and L. Wu, *Inorg. Chem.*, 2015, **54**, 1191–1193.
- 208 M. Martis, K. Mori, K. Fujiwara, W.-S. Ahn and H. Yamashita, *J. Phys. Chem. C*, 2013, **117**, 22805–22810.
- 209 M. Martis, W. Meicheng, K. Mori and H. Yamashita, *Catal. Today*, 2014, **235**, 98–102.
- 210 J. D. Xiao, L. Han, J. Luo, S. H. Yu and H. L. Jiang, *Angew. Chem., Int. Ed.*, 2018, **57**, 1103–1107.
- 211 M. A. Nasalevich, R. Becker, E. V. Ramos-Fernandez, S. Castellanos, S. L. Veber, M. V. Fedin, F. Kapteijn, J. N. Reek, J. Van Der Vlugt and J. Gascon, *Energy Environ. Sci.*, 2015, **8**, 364–375.
- 212 Z. Li, J.-D. Xiao and H.-L. Jiang, *ACS Catal.*, 2016, **6**, 5359–5365.
- 213 K. Meyer, S. Bashir, J. Llorca, H. Idriss, M. Ranocchiari and J. A. van Bokhoven, *Chem.–Eur. J.*, 2016, **22**, 13894–13899.
- 214 B. Zhang, J. Zhang, X. Tan, D. Shao, J. Shi, L. Zheng, J. Zhang, G. Yang and B. Han, *ACS Appl. Mater. Interfaces*, 2018, **10**, 16418–16423.
- 215 F. Li, D. Wang, Q.-J. Xing, G. Zhou, S.-S. Liu, Y. Li, L.-L. Zheng, P. Ye and J.-P. Zou, *Appl. Catal., B*, 2019, **243**, 621–628.
- 216 J. X. Xu, J. Y. Gao, C. Wang, Y. Yang and L. Wang, *Appl. Catal., B*, 2017, **219**, 101–108.
- 217 Z. Wang, C. Li and K. Domen, *Chem. Soc. Rev.*, 2019, **48**, 2109–2125.
- 218 G. Zhou, M.-F. Wu, Q.-J. Xing, F. Li, H. Liu, X.-B. Luo, J.-P. Zou, J.-M. Luo and A.-Q. Zhang, *Appl. Catal., B*, 2018, **220**, 607–614.
- 219 Y. Chen, D. Wang, X. Deng and Z. Li, *Catal. Sci. Technol.*, 2017, **7**, 4893–4904.
- 220 C. A. Trickett, A. Helal, B. A. Al-Maythalyony, Z. H. Yamani, K. E. Cordova and O. M. Yaghi, *Nat. Rev. Mater.*, 2017, **2**, 17045.
- 221 M. B. Ross, *Joule*, 2019, **3**, 1814–1816.
- 222 R. Li, W. Zhang and K. Zhou, *Adv. Mater.*, 2018, **30**, 1705512.
- 223 S. Wu, X. Xing, D. Wang, J. Zhang, J. Chu, C. Yu, Z. Wei, M. Hu, X. Zhang and Z. Li, *ACS Sustainable Chem. Eng.*, 2020, **8**, 148–153.
- 224 Y. Fu, L. Sun, H. Yang, L. Xu, F. Zhang and W. Zhu, *Appl. Catal., B*, 2016, **187**, 212–217.
- 225 T. Toyao, M. Saito, Y. Horiuchi, K. Mochizuki, M. Iwata, H. Higashimura and M. Matsuoka, *Catal. Sci. Technol.*, 2013, **3**, 2092–2097.
- 226 D. Sun, L. Ye and Z. Li, *Appl. Catal., B*, 2015, **164**, 428–432.
- 227 Z. Yang, X. Xu, X. Liang, C. Lei, Y. Cui, W. Wu, Y. Yang, Z. Zhang and Z. Lei, *Appl. Catal., B*, 2017, **205**, 42–54.
- 228 M. Li, H. Huang, J. Low, C. Gao, R. Long and Y. Xiong, *Small Methods*, 2019, **3**, 1800388.
- 229 R. Beranek, *Angew. Chem., Int. Ed.*, 2019, **58**, 16724–16729.
- 230 H. Huang, X.-S. Wang, D. Philo, F. Ichihara, H. Song, Y. Li, D. Li, T. Qiu, S. Wang and J. Ye, *Appl. Catal., B*, 2020, **267**, 118686.
- 231 H. Guo, D. Guo, Z. Zheng, W. Weng and J. Chen, *Appl. Organomet. Chem.*, 2015, **29**, 618–623.
- 232 R. M. Abdelhameed, M. M. Simoes, A. M. Silva and J. Rocha, *Chem.–Eur. J.*, 2015, **21**, 11072–11081.
- 233 X. Yuan, H. Wang, Y. Wu, G. Zeng, X. Chen, L. Leng, Z. Wu and H. Li, *Appl. Organomet. Chem.*, 2016, **30**, 289–296.
- 234 H. Wang, X. Yuan, Y. Wu, G. Zeng, H. Dong, X. Chen, L. Leng, Z. Wu and L. Peng, *Appl. Catal., B*, 2016, **186**, 19–29.
- 235 J. Xu, J. Gao, C. Wang, Y. Yang and L. Wang, *Appl. Catal., B*, 2017, **219**, 101–108.
- 236 H. Wang, X. Yuan, Y. Wu, G. Zeng, X. Chen, L. Leng and H. Li, *Appl. Catal., B*, 2015, **174**, 445–454.
- 237 R. M. Abdelhameed, D. M. Tobaldi and M. Karmaoui, *J. Photochem. Photobiol., A*, 2018, **351**, 50–58.
- 238 R. Kaur, A. Rana, R. K. Singh, V. A. Chhabra, K.-H. Kim and A. Deep, *RSC Adv.*, 2017, **7**, 29015–29024.
- 239 M. J. Islam, H. K. Kim, D. A. Reddy, Y. Kim, R. Ma, H. Baek, J. Kim and T. K. Kim, *Dalton Trans.*, 2017, **46**, 6013–6023.
- 240 V. Benoit, R. S. Pillai, A. Orsi, P. Normand, H. Jobic, F. Nouar, P. Billefont, E. Bloch, S. Bourrelly and T. Devic, *J. Mater. Chem. A*, 2016, **4**, 1383–1389.
- 241 M. W. Anjum, B. Bueken, D. De Vos and I. F. Vankelecom, *J. Membr. Sci.*, 2016, **502**, 21–28.

- 242 Z. H. Rada, H. R. Abid, J. Shang, Y. He, P. Webley, S. Liu, H. Sun and S. Wang, *Fuel*, 2015, **160**, 318–327.
- 243 J. H. Im, N. Ko, S. J. Yang, H. J. Park, J. Kim and C. R. Park, *New J. Chem.*, 2014, **38**, 2752–2755.
- 244 S. Vaesen, V. Guillerm, Q. Yang, A. D. Wiersum, B. Marszalek, B. Gil, A. Vimont, M. Daturi, T. Devic and P. L. Llewellyn, *Chem. Commun.*, 2013, **49**, 10082–10084.
- 245 F. Vermoortele, M. Maes, P. Z. Moghadam, M. J. Lennox, F. Ragon, M. Boulhout, S. Biswas, K. G. Laurier, I. Beurroies and R. Denoyel, *J. Am. Chem. Soc.*, 2011, **133**, 18526–18529.
- 246 F. Zhong, C. Li, Y. Xie, H. Xu and J. Gao, *J. Solid State Chem.*, 2019, **278**, 120892.
- 247 H. Xu, J. Gao, X. Qian, J. Wang, H. He, Y. Cui, Y. Yang, Z. Wang and G. Qian, *J. Mater. Chem. A*, 2016, **4**, 10900–10905.
- 248 F. Zhong, X. Zhang, C. Zheng, H. Xu, J. Gao and S. Xu, *J. Solid State Chem.*, 2020, **288**, 121391.
- 249 D. Jin, Q. Xu, L. Yu and X. Hu, *Microchim. Acta*, 2015, **182**, 1885–1892.
- 250 A. V. Vinogradov, H. Zaake-Hertling, E. Hey-Hawkins, A. V. Agafonov, G. Seisenbaeva, V. Kessler and V. V. Vinogradov, *Chem. Commun.*, 2014, **50**, 10210–10213.
- 251 W. Liu, Y. Mi, Z. Weng, Y. Zhong, Z. Wu and H. Wang, *Chem. Sci.*, 2017, **8**, 4285–4291.
- 252 C. T. Saouma, C.-C. Tsou, S. Richard, R. Ameloot, F. Vermoortele, S. Smolders, B. Bueken, A. G. DiPasquale, W. Kaminsky, C. N. Valdez, D. E. De Vos and J. M. Mayer, *Chem. Sci.*, 2019, **10**, 1322–1331.
- 253 U. Ryu, S. Jee, J.-S. Park, I. K. Han, J. H. Lee, M. Park and K. M. Choi, *ACS Nano*, 2018, **12**, 4968–4975.
- 254 W. P. Mounfield III, C. Han, S. H. Pang, U. Tumuluri, Y. Jiao, S. Bhattacharyya, M. R. Dutzer, S. Nair, Z. Wu and R. P. Lively, *J. Phys. Chem. C*, 2016, **120**, 27230–27240.
- 255 S. Van der Perre, A. Liekens, B. Bueken, D. E. De Vos, G. V. Baron and J. F. Denayer, *J. Chromatogr. A*, 2016, **1469**, 68–76.
- 256 E. Vlasova, S. Yakimov, E. Naidenko, E. Kudrik and S. Makarov, *Food Chem.*, 2016, **190**, 103–109.
- 257 I. Ahmed, N. A. Khan, J. W. Yoon, J.-S. Chang and S. H. Jhung, *ACS Appl. Mater. Interfaces*, 2017, **9**, 20938–20946.
- 258 M. Sohail, Y.-N. Yun, E. Lee, S. K. Kim, K. Cho, J.-N. Kim, T. W. Kim, J.-H. Moon and H. Kim, *Cryst. Growth Des.*, 2017, **17**, 1208–1213.
- 259 G. Ye, Y. Gu, W. Zhou, W. Xu and Y. Sun, *ACS Catal.*, 2020, **10**, 2384–2394.
- 260 A. M. Fracaroli, H. Furukawa, M. Suzuki, M. Dodd, S. Okajima, F. Gándara, J. A. Reimer and O. M. Yaghi, *J. Am. Chem. Soc.*, 2014, **136**, 8863–8866.
- 261 R. W. Flaig, T. M. Osborn Popp, A. M. Fracaroli, E. A. Kapustin, M. J. Kalmutzki, R. M. Altamimi, F. Fathieh, J. A. Reimer and O. M. Yaghi, *J. Am. Chem. Soc.*, 2017, **139**, 12125–12128.
- 262 K. T. Butler, C. H. Hendon and A. Walsh, *J. Am. Chem. Soc.*, 2014, **136**, 2703–2706.